THE ASTRONOMICAL JOURNAL, 116:293–321, 1998 July

EXTERNALLY ILLUMINATED YOUNG STELLAR ENVIRONMENTS IN THE ORION NEBULA: *HUBBLE SPACE TELESCOPE* PLANETARY CAMERA AND ULTRAVIOLET OBSERVATIONS

JOHN BALLY,[1,2] RALPH S. SUTHERLAND,[3] DAVID DEVINE,[2,4] AND DOUG JOHNSTONE[5]
Received 1997 September 29; revised 1998 April 1

ABSTRACT

We present new 0.″05 resolution (22 AU) narrowband *Hubble Space Telescope* Planetary Camera images of externally illuminated young stellar objects embedded in the Orion Nebula. We also present 0.″02 resolution (9 AU) UV images of seven externally illuminated protostellar environments and the first UV spectra that cover the spectral range between 1400 and 3000 Å. We discuss 43 objects for which the angular resolution has been improved over previous data by more than a factor of 2. These young stellar objects are either embedded inside the Orion Nebula and externally illuminated by the Trapezium stars or located in front of the nebula and seen in silhouette. The visibility of young stars surrounded by diffuse matter is dominated by intense line emission from ionization fronts (IFs) propagating into material photoablated from circumstellar disks by soft UV radiation. Near the Trapezium stars, the electron density at these IFs is around 10^5 to 10^6 cm^{-3} and the radial intensity profiles of emission lines decrease roughly as r^{-3}, consistent with an approximately constant-velocity diverging flow with an r^{-2} density profile. However, some radial intensity profiles are better fitted with an exponential function. Low ionization fraction near the IF and the heating and acceleration of the photoablation flow can explain deviations from the r^{-3} intensity profiles. Many young stars located within 30″ of θ^1 Ori C are surrounded by concentric arcs of [O III] and Hα emission located 0.″5 to 3″ from the IF facing θ^1 Ori C. These arcs may trace bow shocks formed by the interaction of the expanding photoablation flow with the fast stellar wind from θ^1 Ori C. The [O III] emission may be enhanced by UV radiation from θ^1 Ori C, thermal conduction, and/or turbulent mixing of weakly shocked, photoablated gas with the thermalized shocked stellar wind. About 30% of the bright externally illuminated young stellar objects contain dark regions seen in silhouette against background nebular emission in Hα and the forbidden transitions of common ions that may trace circumstellar protoplanetary disks. In some sources, the regions seen in silhouette in Hα and ionic transitions are *bright* in the 6300 Å [O I] line. Most externally illuminated young stellar objects have dusty tails pointing radially away from the source of ionizing photons. Tails have an average length of 500 AU, independent of the projected distance from θ^1 Ori C, are limb-brightened in emission lines, and are sometimes seen in silhouette against background nebular light, indicating that they contain large column densities of gas and dust. We discuss a variety of tail formation mechanisms and conclude that initial conditions probably play a key role in their formation. The large fraction of young stellar objects with extended circumstellar structure, the mass limits on this structure, and the estimated mass-loss rates are combined to produce an estimate for the photoionization age of the Orion Nebula. The derived photoionization age of the Orion Nebula is less than 10^5 yr and possibly as short as 10^4 yr.

Key words: ISM: individual (Orion Nebula) — stars: formation — stars: pre–main-sequence

1. INTRODUCTION

The Orion Nebula (M42, NGC 1976) is the nearest H II region and site of ongoing massive star formation. Located at a distance of about 430 pc (Warren & Hesser 1977), it is the "Rosetta stone" for the study of young stellar objects (YSOs). The principal sources of ionizing radiation are the O6p star θ^1 Orionis C in the Trapezium cluster and the O9 star θ^2 Orionis A located several arcminutes to the south. Their youth and proximity make the Orion Nebula the highest apparent surface brightness H II region in the solar vicinity. Near-infrared images of the nebula and the molecular cloud core that lies less than 1 pc behind it reveal an exceptional concentration of young stars (McCaughrean 1988; Allen & Burton 1993; McCaughrean & Stauffer 1994; Prosser et al. 1994). The Trapezium cluster contains over 700 stars that formed in a region less than 0.5 pc in diameter. Modeling of the stellar distribution has led to an estimated core density of about 50,000 stars per cubic parsec, which corresponds to an average nearest neighbor distance of about 6000 AU (McCaughrean & Stauffer 1994). The ages of several hundred stars in the Trapezium cluster have been estimated by fitting theoretical isochrones to the observed H-R diagram of the cluster (Herbig & Terndrup 1986; Jones & Walker 1988; Hillenbrand 1997). The

[1] Department of Astrophysical and Planetary Sciences and Center for Astrophysics and Space Astronomy, University of Colorado, Boulder, CO 80309-0389; bally@casa.colorado.edu.

[2] Visiting Astronomer, Kitt Peak National Observatory, National Optical Astronomy Observatories, operated by the Association of Universities for Research in Astronomy, Inc., under cooperative agreement with the National Science Foundation.

[3] Astrophysical Theory Centre and Mount Stromlo and Siding Spring Observatories, Australian National University, Canberra, ACT 0200, Australia; ralph.sutherland@anu.edu.au.

[4] NASA Goddard Space Flight Center, Code 681, Greenbelt, MD 20771; devine@h2.gsfc.nasa.gov.

[5] Canadian Institute for Theoretical Astrophysics, University of Toronto, 60 St. George Street, Toronto, ON M5S 3H8, Canada; johnstone@cita.utoronto.ca.

median cluster age is between 3×10^5 and 10^6 yr, with few stars older than 10^6 yr. Because the birth of the massive stars probably halted further star formation within the ionized region, the photoionization age of the nebula must be less than 3×10^5 yr, making it one of the youngest H II regions known.

Young stars that have formed from the Orion molecular core (OMC-1) have been uncovered by the advancing H II region and are now embedded in its interior. The remnants of the circumstellar environments from which these young stars were born are illuminated from the outside by the intense radiation fields of the massive stars. Since the *Hubble Space Telescope* (*HST*) Faint Object Camera images can resolve structure as small as 9 AU in the Orion Nebula, *HST* provides an opportunity to investigate the properties of young stars and their environments, including the dense protoplanetary accretion disks, with more than 1 order of magnitude improvement in angular resolution over other techniques, such as millimeter-wavelength interferometry or near-infrared imaging.

Externally illuminated YSOs were first detected in the Orion Nebula by Laques & Vidal (1979), who found seven compact knots bright in Hα in the immediate vicinity of the Trapezium cluster (the LV sources). Free-free radio continuum emission from these objects and other subarcsecond-diameter condensations both inside the H II region and embedded in the molecular gas in the background were detected by the Very Large Array (VLA) radio telescope in the mid-1980s by Churchwell et al. (1987) and Garay, Moran, & Reid (1987). More detailed radio observations (Felli et al. 1993a, 1993b) resulted in the discovery of over 30 compact free-free emitting sources. Some are resolved and exhibit cometary tails pointing away from Trapezium while others show arc-shaped emission facing these hot stars.

McCaughrean (1988) obtained high-quality near-infrared images of the Orion Nebula and demonstrated that nearly all compact VLA sources coincide with infrared sources. O'Dell, Wen, & Hu (1993) detected intense line emission that wraps around the residual dense gas that surrounds over 50 YSOs born from the Orion molecular cloud. The *HST* observations support the identification of these objects as externally illuminated circumstellar environments. O'Dell et al. (1993) coined the phrase "proplyd" (an acronym for "protoplanetary disk") to describe them. After the first *HST* service mission, in 1993 December, the Orion Nebula was reobserved by O'Dell & Wen (1994). The dramatic improvement in the performance of *HST* led to the detection of previously unseen features and many new YSOs, including six objects that lie in the foreground and are seen only in silhouette. Several of the bright objects and some of the silhouetted objects have been detected at 10 μm in emission (Hayward, Houck, & Miles 1994; Hayward & McCaughrean 1997), providing further evidence that these YSOs are surrounded by disks. A catalog of 153 externally illuminated YSOs was presented by O'Dell & Wong (1996), and a detailed analysis of the silhouetted objects was given by McCaughrean & O'Dell (1996).

In this paper, we present follow-up observations of the externally illuminated YSOs in the Orion Nebula obtained with *HST* in 1994 and 1995 with the PC portion of the Wide Field Planetary Camera 2 (WFPC2), with the Faint Object Camera (FOC), and with the Faint Object Spectrograph (FOS). Our observations and those of O'Dell & Wen (1994) and McCaughrean & O'Dell (1996) were carefully coordinated to maximize the coverage of the core of the Orion Nebula and to obtain the highest angular resolution observations possible of many YSOs. The final mosaic of the Orion Nebula, which has appeared in various publications, used the combined observations obtained from our and O'Dell's observing programs.

2. OBSERVATIONS

2.1. *HST*

We observed four fields near Trapezium with the 0.″05 angular resolution of the Planetary Camera (PC) portion of WFPC2 on *HST* on 1995 March 17. The angular resolution of these images is more than a factor of 2 better than previous WF camera images and provide 22 AU linear resolution at a distance of 430 pc, which we adopt for the Orion Nebula. Observations were obtained through narrowband filters centered on the [S II], [N II], Hα, [O I], and [O III] lines and in an emission-line–free continuum channel. Three identical exposures were obtained through each filter for each pointing. Since the set of three images in each filter was always obtained within the same orbit and using one set of guide stars, the registration of star images on individual exposures was found to be better than 0.1 pixels. Data received from STScI had been flat-field–corrected and calibrated for a variety of effects by the standard WFPC2 processing pipeline.

The three identical exposures were median-combined to yield a single image for each filter and each target. This procedure removed most cosmic rays from the data. Remaining cosmic rays, hot pixels, and other artifacts were eliminated by hand. We used stars in the images to register frames taken through different filters. Three-color 24 bit red-green-blue (RGB) images were made with Adobe Photoshop by combining data taken through three different filters in various combinations. Coordinates for objects listed in Tables 2 and 3 below were obtained with the STSDAS routine METRIC, which converts raw pixel coordinates into distortion-corrected J2000.0 coordinates referenced to the Guide Star Catalog.

The data numbers (DNs) were converted into spectral line flux densities (F_λ) in units of ergs $\mathrm{cm}^{-2}\ \mathrm{s}^{-1}\ \mathrm{pixel}^{-1}$ by

$$F_\lambda = \frac{N_e}{A_T}\frac{hc}{\lambda}\frac{1}{QT_{\max}}, \quad (1)$$

where N_e is the number of electrons detected per second by each pixel in the focal plane of the telescope and is given by $\mathrm{DN}G/t_{\exp}$, where G is the gain (in electrons per DN) and $t_{\exp}$ is the exposure time in seconds. A_T is the effective aperture, Q is the throughput efficiency of telescope, corrective optics, and camera, and $T_{\max}$ is the filter transmission at the wavelength of a spectral line.

This method is only approximate, since it assumes that contamination by additional lines and continuum within the passband can be ignored. Therefore, this method works only when the emission in the filter is dominated by the observed emission line. For example, the F656N filter used to observe Hα is contaminated by partial transmission of the two [N II] lines near the Hα line. For equal fluxes in the [N II] and Hα lines, the resulting error in the Hα flux would be about 15%. However, typically the [N II] lines are more than 3–10 times fainter than Hα, and the resulting error in the Hα flux is less than about 5%. Since the [N II] filter only transmits about 2% of the incident Hα flux, the contami-

TABLE 1

OBSERVATIONS OF THE ORION NEBULA

Target	α (B1950.0)	δ (B1950.0)	Filter/Grating	Exposure (s)	Comments
			WFPC2 PC1[a]		
LV 3	5 32 48.83	−5 25 10.07	F673N	3 × 100	Both [S II] lines
			F658N	3 × 100	[N II]
			F656N	3 × 60	Hα
			F631N	3 × 100	[O I]
			F502N	3 × 100	[O III]
			F547M	3 × 30	Continuum
HST 1	5 32 50.23	−5 25 33.7	F673N	3 × 180	Both [S II] lines
			F658N	3 × 180	[N II]
			F656N	3 × 60	Hα
			F631N	3 × 100	[O I]
			F502N	3 × 180	[O III]
			F547M	3 × 30	Continuum
HST 3	5 32 48.49	−5 25 43.5	F673N	3 × 100	Both [S II] lines
			F658N	3 × 100	[N II]
			F656N	3 × 60	Hα
			F631N	3 × 100	[O I]
			F502N	3 × 100	[O III]
			F547M	3 × 30	Continuum
HST 10	5 32 50.75	−5 26 06.1	F673N	3 × 180	Both [S II] lines
			F658N	3 × 180	[N II]
			F656N	3 × 60	Hα
			F631N	3 × 180	[O I]
			F502N	3 × 180	[O III]
			F547M	3 × 30	Continuum
			FOC/96[b]		
LV 6–VLA 10 NW	5 32 48.32	−5 25 18.0	F253M	2 × 60	C II]
			F231M	2 × 60	O II]
			F190M	2 × 60	C III
HST 16	5 32 50.89	−5 25 57.5	F253M	2 × 60	C II]
			F231M	2 × 60	O II]
			F190M	2 × 60	C III
HST 10	5 32 50.75	−5 26 06.1	F253M	2 × 60	C II]
			F231M	2 × 60	O II]
			F190M	2 × 60	C III
			FOS[c]		
HST 4 (LV 6)	5 32 48.32	−5 25 20.15	G130H	300	On-source
			G190H	300	
			G270H	300	
HST 4 (SKY 1)	5 32 48.39	−5 25 20.15	G130H	300	1″ east
			G190H	300	
			G270H	300	
HST 3	5 32 48.49	−5 25 43.5	G130H	300	On-source
			G190H	300	
			G270H	300	
HST 3 (SKY 2)	5 32 48.52	−5 25 42.56	G130H	300	1.″0 off-source
			G190H	300	
			G270H	300	
HST 3 (SKY 3)	5 32 48.54	−5 25 41.62	G130H	300	2.″0 off-source
			G190H	300	
			G270H	300	

NOTE.—Units of right ascension are hours, minutes, and seconds, and units of declination are degrees, arcminutes, and arcseconds.

[a] All WFPC2 observations were obtained on 1995 March 21.

[b] All FOC observations were obtained on 1994 October 21.

[c] All FOS observations were obtained on 1994 October 8. The FOS aperture used is circular and 1″ in diameter.

nation by Hα may raise the estimated [N II] flux by about 20% at most. None of the other narrowband filters suffer serious line contamination; however, serious contamination can arise in the presence of bright continuum sources such as stars. We have attempted to use the F547M data to remove the continuum sources from the narrowband images. Unfortunately, variations in the intrinsic colors of stars in the field are large, and the results of global image subtractions are less than satisfactory. Therefore, in this paper we restrict our analysis to emission-line surface brightness measurements of regions that are sufficiently distant from each continuum source so that continuum contamination is small. We leave more sophisticated analyses in which we attempt to compute precise continuum-corrected fluxes to future work. The fluxes reported in Table 3 below are restricted to regions of the images well away

from stars, and we estimate that the quoted surface brightness per pixel is accurate to about 5%–25%.

UV images of two fields were obtained in 1994 November using FOC. The FOC pixel scale of 0.″014 corresponds to a linear scale of about 6 AU in the Orion Nebula. We obtained images through a medium passband filter (F253M) that transmits the semiforbidden lines O II] (2326 Å) and C II] (2470 Å). We also obtained images through a medium-band filter (F190M) centered on the 1900 Å C III line. A preliminary report of these observations was presented by Bally, Devine, & Sutherland (1995).

Moderate-resolution ($R = 1300$) UV spectra were obtained of the externally illuminated YSOs 158−327 (LV 6, HST 4) and 159−350 (HST 3) and three positions in the nebula near these objects in 1994 December with FOS using a 1″ circular aperture. Three different FOS gratings (G130H, G190H, and G270H) were used to cover the spectrum from 1150 to 3300 Å. Table 1 provides a summary of these observations including exposure dates, times, filters, number of pointings, and pointing coordinates.

3. OBSERVATIONAL RESULTS

3.1. *HST FOS Spectra*

Two externally illuminated YSOs, 158−327 (HST 4, LV 6) and 159−350 (HST 3) and three adjacent SKY positions located several arcseconds away were targeted for UV spectroscopic observations with FOS. Three settings of FOS covered the spectral range from 1150 to 3300 Å. Details of the observations are given in Table 1. Figure 1 shows the FOS spectra of the fields listed in Table 1. The results of the observations, including the peak surface brightness measured in our aperture in the brighter emission lines and the continuum level at three wavelengths, are given in Table 2 for both externally illuminated YSOs and the three adjacent SKY positions. The spectral line fluxes have been continuum-subtracted. The exact pointing of these observations is uncertain by about 0.″2 since *HST* was able to track on only one guide star. However, both targets are sufficiently small that in the on-source pointings the slits contained the bright emission from the externally illuminated YSOs, while the off-source pointings (1″ away) were not contaminated by this emission and, therefore, sample the nebular background. Emission from the externally illuminated YSOs was detected in C III, C II], O II], and Mg II.

Continuum emission is observed in all spectra; however, the continuum toward the externally illuminated YSOs is marginally brighter than toward the adjacent sky reference positions. The UV continuum is much brighter than the total emission from spectral lines over the observed portion of the spectrum. The continuum is very blue and reaches maximum intensity [(2–7) × 10^{-14} ergs cm^{-2} s^{-1} $Å^{-1}$ at 1300 Å] at the shortest observed wavelengths, where it is about 10 times stronger than at 3000 Å.

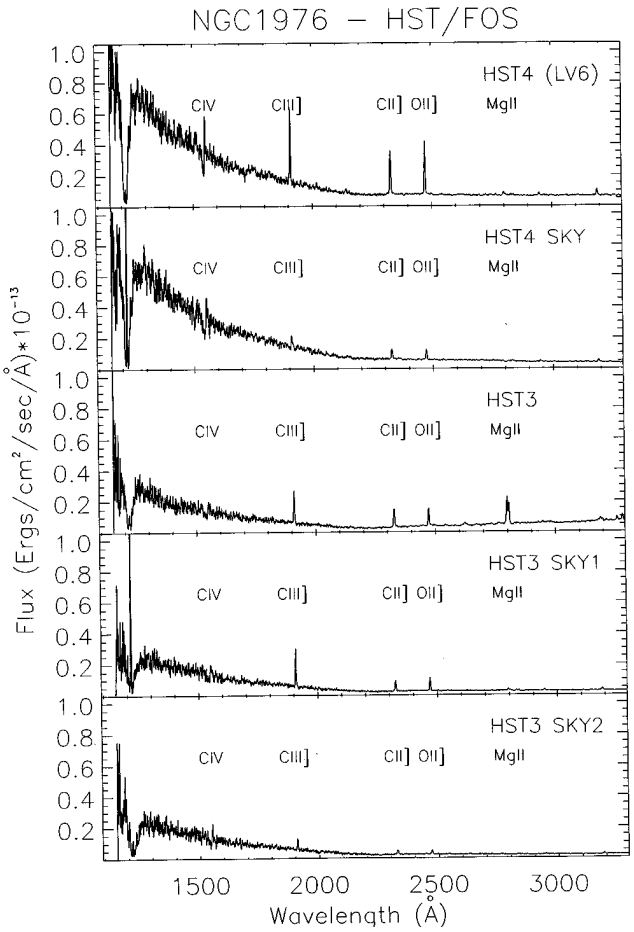

FIG. 1.—FOS spectra showing three separate settings of FOS and five pointings listed in Tables 1 and 2. *Top to bottom*: FOS spectrum of 158−327 (LV 6), FOS spectrum of the nebula at position listed as LV 6 SKY 1 in Table 2 near 158−327 (LV 6), FOS spectrum of 159−350 (HST 3), FOS spectrum of sky nebula at position listed as HST 3 SKY 1 in Table 2 near 159−350 (HST 3), and FOS spectrum of sky nebula at position listed as HST 3 SKY 2 in Table 2 near 159−350 (HST 3).

The Lyα profile exhibits a broad absorption dip toward all observed positions. A strong emission spike, centered in the absorption feature, is observed toward all SKY positions but is absent or much weaker toward the externally illuminated YSOs. A P Cygni profile is seen in the 1549 Å C IV line in the spectrum of 158−327 and faintly in the adjacent SKY position.

The C III line is visible in all of our spectra and is 5 times stronger toward the externally illuminated YSO 158−327

TABLE 2

SUMMARY OF FOS OBSERVATIONS

Source	Lyα 1216 Å	Continnum 1300 Å	C III λ1909	Continuum 2000 Å	C II] λ2329	[O II] λ2471	Mg II λ2796/λ2803	Continuum 3000 Å	He I λ2946	He I λ3189
158−327 (LV 6)	15	70	50	12	35	42	4	6.5	2	5
LV 6 SKY 1.....	150	65	7	12	6	6.5	0	4	1.2	2
159−350 (HST 3).....	25	25	27	5	16	18	26	5	0	2.5
HST 3 SKY 1	145	20	30	5	8.5	12	3	2.5	3	4
HST 3 SKY 2	14	20	11	4	2.8	2.6	0	2	0.5	1

NOTES.—Flux units are in 10^{-15} ergs cm^{-2} s^{-1} $Å^{-1}$ in a 1″ diameter circular aperture. Lyα has a broad and saturated absorption dip. The quoted fluxes refer to the central emission spike that is seen toward the sky reference positions. Line fluxes are continuum-subtracted.

(HST 4, LV 6) than the nearby SKY reference position. This line was also detected in the spectrum of 159−350 (HST 3) and the two adjacent reference positions. The C III line is fainter toward the first reference position but brighter toward the second. The source 158−327 lies at a projected distance of 10″.6 from θ^1 Ori C, while 159−350 lies about 38″.5 from θ^1 Ori C, so the strong C III in the first object may be due to its proximity to θ^1 Ori C.

The C II] and O II] lines have large, similar fluxes in both externally illuminated YSOs. The two lines are significantly brighter toward the externally illuminated YSO than the surrounding nebula (about a factor of 10 in 158−327 and about a factor of 2–5 in 159−350). The Mg II resonance line is faint in the externally illuminated YSOs and not visible in the sky reference positions. Two other faint emission lines, which are produced by neutral helium, appear near 2950 and 3190 Å.

3.2. *HST Planetary Camera and FOC Images*

Figures 2 through 5 show the PC images of the externally illuminated YSOs embedded in the Orion Nebula near the Trapezium stars. The color images are RGB composites in which the figure captions describe the color assignments.

Figure 2 is centered on the Trapezium and contains the original objects discovered by Laques & Vidal (1979). About a dozen externally illuminated YSOs are visible in this image. All have very bright emission-line fronts on the side facing θ^1 Ori C (overexposed in this reproduction) and have tails ranging in length from 0″.4 to over 2″ that point radially away from θ^1 Ori C. The tails are limb-brightened in low-excitation lines, and parts of the tails are visible in silhouette against the nebular background in [O III] and [N II]. Some tails (cf. 158−327 = LV 6 = HST 4) show

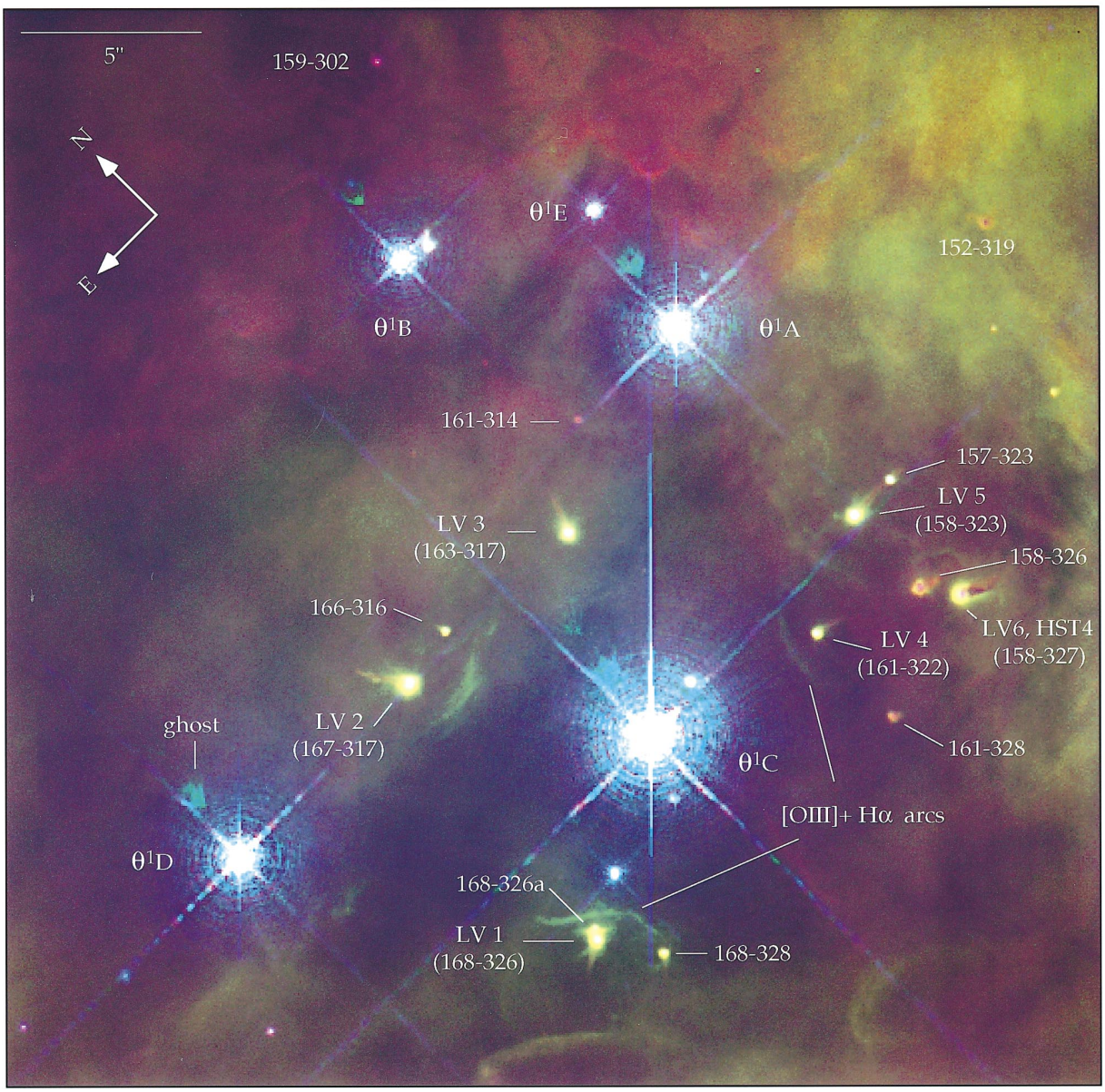

FIG. 2.—Trapezium region as a color mosaic of the PC images from the Cycle 4 WFPC2 *HST* observations of the Orion Nebula in narrowband filters. Red is [N II], green is Hα, and blue is [O I].

slight wiggles and other distortions near their ends, and some point a few degrees away from θ^1 Ori C. Arcs consisting of bright [O III] and Hα emission are seen on the sides of the externally illuminated YSOs facing θ^1 Ori C and, in every case, are concave toward the externally illuminated YSOs and convex toward θ^1 Ori C. The [O III] arcs are displaced from the externally illuminated YSO ionization fronts (IFs) by 1″–3″ toward θ^1 Ori C.

Figure 3 is centered about 30″ southeast of the Trapezium, where there is a prominent ring of externally illuminated YSOs (which we dub "Corona Ori"). Of the nine bright objects in the ring, all but two exhibit prominent tails with lengths ranging from under 1″ to 4″. On average, these objects are larger than those closer to θ^1 Ori C. The object in the center of the field, 177−341 (HST 1), sports the largest emission-line crescent (which we will show to be an IF) and the longest tail. The parts of the IFs that face θ^1 Ori C are nearly hemispherical. The tails are strongly limb-brightened in most emission lines, especially in [N II], and tend to be wider in the higher excitation species than in the lower excitation lines. The tails connect smoothly to the hemispherical IFs and become progressively narrower "downwind." Most tails end in very sharp points that have radii of curvature less than 0.″1. The second brightest object in Figure 3, 170−337 (HST 2), has a filament of [O III] emission that extends directly from the star to about 0.″5 beyond the projected edge of the IF facing θ^1 Ori C. A chain of [O III]-bright knots that are probably Herbig-Haro (HH) objects lies several arcseconds farther northeast, roughly along the axis of the filament. As discussed by O'Dell et al. (1997), these [O III] knots are redshifted by about 100 km s^{-1} with respect to the nebular emission. The source 171−340 (HST 11) is a stubby, nearly round object several arcseconds south of 170−337. Unlike most YSOs close to Trapezium, it exhibits a very stubby tail and a prominent silhouetted disk in Hα, [N II], and [O III].

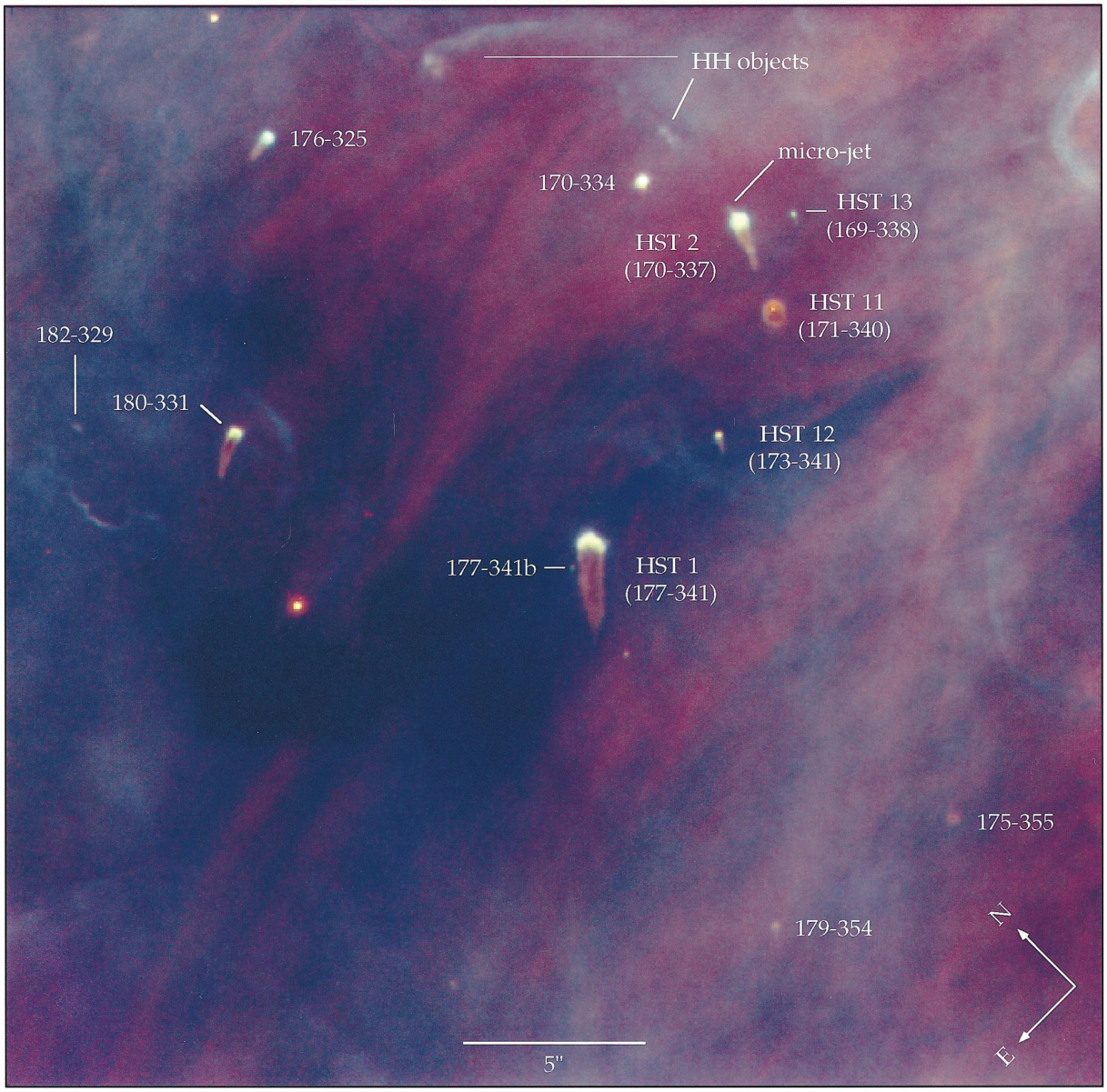

FIG. 3.—Same as Fig. 2, but for the "Corona Ori" region, about 30″ south of Trapezium. Red is [N II], green is Hα, and blue is [O III].

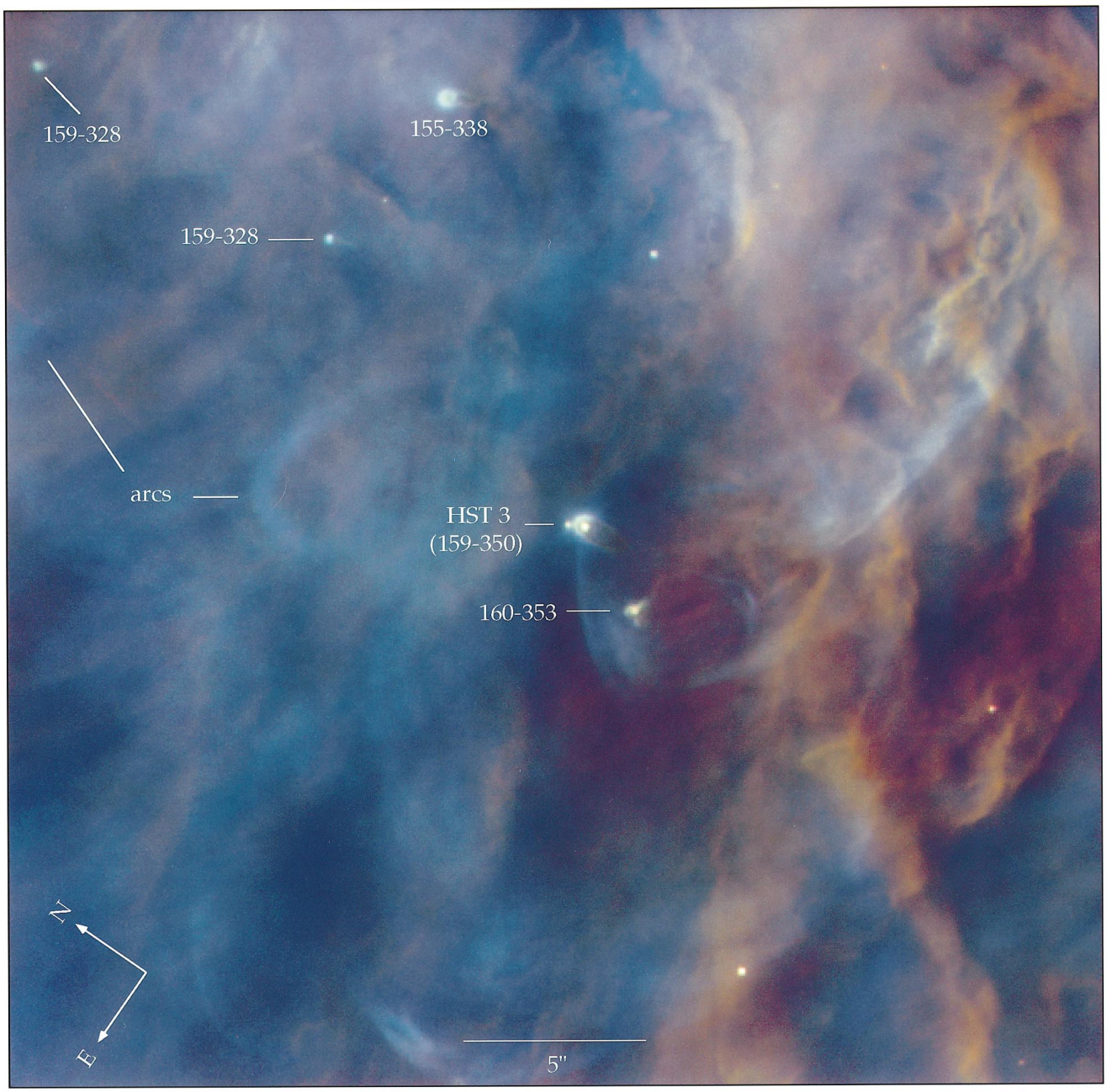

FIG. 4.—Same as Fig. 2, but for the region around HST 3

Figure 4 shows the field centered on the bright object 159−350 (HST 3), one of the most luminous low-mass members of the Trapezium cluster, located about 30″ south of θ^1 Ori C. An unusual externally illuminated YSO, 160−353 (HST 6), which has a cloverleaf geometry, lies about 4″ to the south of 159−350. The object 159−350 (HST 3) lies near the axes of two chains of [O III] bright arcs, one of which extends to the northeast toward "Corona Ori" at intervals of about 10″ while the other extends along a northwest-southeast axis. Unlike the [O III] arcs that are centered on the externally illuminated YSOs near Trapezium, these arcs are not centered on any visible object and do not face θ^1 Ori C.

Figure 5 shows the field centered on 182−413 (HST 10), about 60″ to the south of Trapezium, which resembles Herbig's "interstellar teardrops" seen in the Rosette Nebula (Herbig 1974). This field also contains 183−405 (HST 16), the first of the dark silhouettes to be recognized (O'Dell & Wen 1994) that do not show any evidence of external ionization. None of the externally illuminated YSOs in this field, or for that matter any other field at a comparable projected distance from Trapezium, have

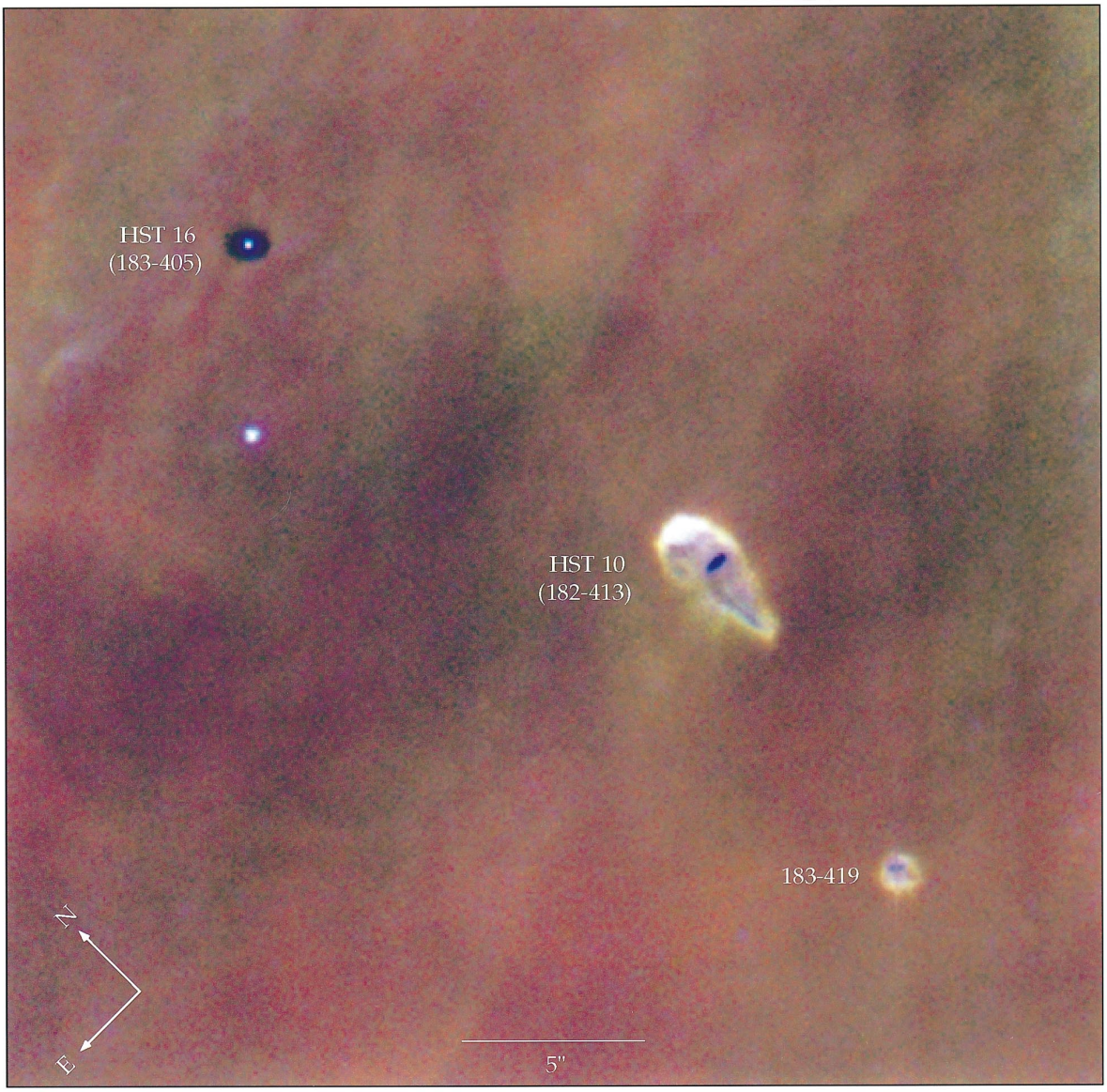

FIG. 5.—Same as Fig. 2, but for the field containing HST 10 and HST 16. Red is [N II], green is Hα, and blue is [O I].

associated [O III] + Hα arcs. The radii of the IFs in this field are on average larger than the IFs associated with the externally illuminated YSOs closer to θ^1 Ori C, and the tails tend to be stubby.

The three largest bright, externally illuminated YSOs in this field each contains opaque regions interior to the IFs. These regions are seen in silhouette against background light in Hα and the forbidden lines of ionized species. However, in the 6300 Å [O I] line the silhouetted regions are bright and seen in *emission.*

Figure 6 shows a color composite mosaic of the Orion Nebula core using all of the WFPC2 PC and WF images from our program. This figure illustrates the general appearance of the nebula's core and contains several additional objects that we discuss but which were not included in our PC fields of view. One of the largest externally illuminated YSOs discovered to date, 142−301, lies about 40″ northwest of θ^1 Ori C (see Fig. 7). We first detected this object from the ground on images taken in 1994 January with the 3.5 m New Technology Telescope at the European Southern Obervatory, La Silla, Chile, in 0.″6 seeing. This object has a tail nearly 4″ long that comes to a very sharp point downstream from θ^1 Ori C. It is one of the few bright, externally illuminated YSOs that does not have a hemispherical IF facing the bright star. The IF looks very flat and sharp on the side facing the Trapezium cluster. Figure 6 also shows the largest pure silhouette, 114−426, located 100″ southwest of θ^1 Ori C.

Figure 7 shows a selection of externally illuminated YSOs in each of the six filters. The objects are arranged by wavelength (increasing to the right) and projected distance from θ^1 Ori C (increasing toward the bottom). From top to bottom, the different rows show the following objects:

1. The 168−326AB binary (LV 1), located at a projected distance of 6.″3 from θ^1 Ori C. Both stars are surrounded by

FIG. 6.—Same as Fig. 2, but for the mosaic obtained by combining all of our Cycle 4 WFPC2 observations. The orientation of this image is as in Figs. 3–5. Red is [N II], green is Hα, and blue is [O III].

prominent [O III] + Hα arcs, with the brighter arc lying between the two sources. The tails point directly away from θ^1 Ori C.

2. The source 163−317 (LV 3), located at a projected distance of 6.″9 from θ^1 Ori C. A long, skinny tail points directly away from θ^1 Ori C.

3. The object 167−317 (LV 2), located at a projected distance of 7.″8 from θ^1 Ori C (the brighter object), and 166−316, located 7.″2 from θ^1 Ori C (fainter object). Both objects have prominent [O III] + Hα arcs facing θ^1 Ori C and skinny tails pointing radially away.

4. The 158−327 (*left*) and 158−325 (*right*; this object is also known as LV 6 = HST 4) group, at a projected distance of 9.″6 and 10.″3 from θ^1 Ori C. Both objects show central silhouettes in [O III]. Note the apparent bend in the tail of 158−325 on the right.

5. The object 170−337 (HST 2), which powers a stellar microjet (O'Dell et el. 1997), is located at the top left at a projected distance of 16.″1 from θ^1 Ori C. The small faint object to the right is 169−338 (HST 13); 171−340 (HST 11), a much fainter object, contains an embedded silhouette in [O III].

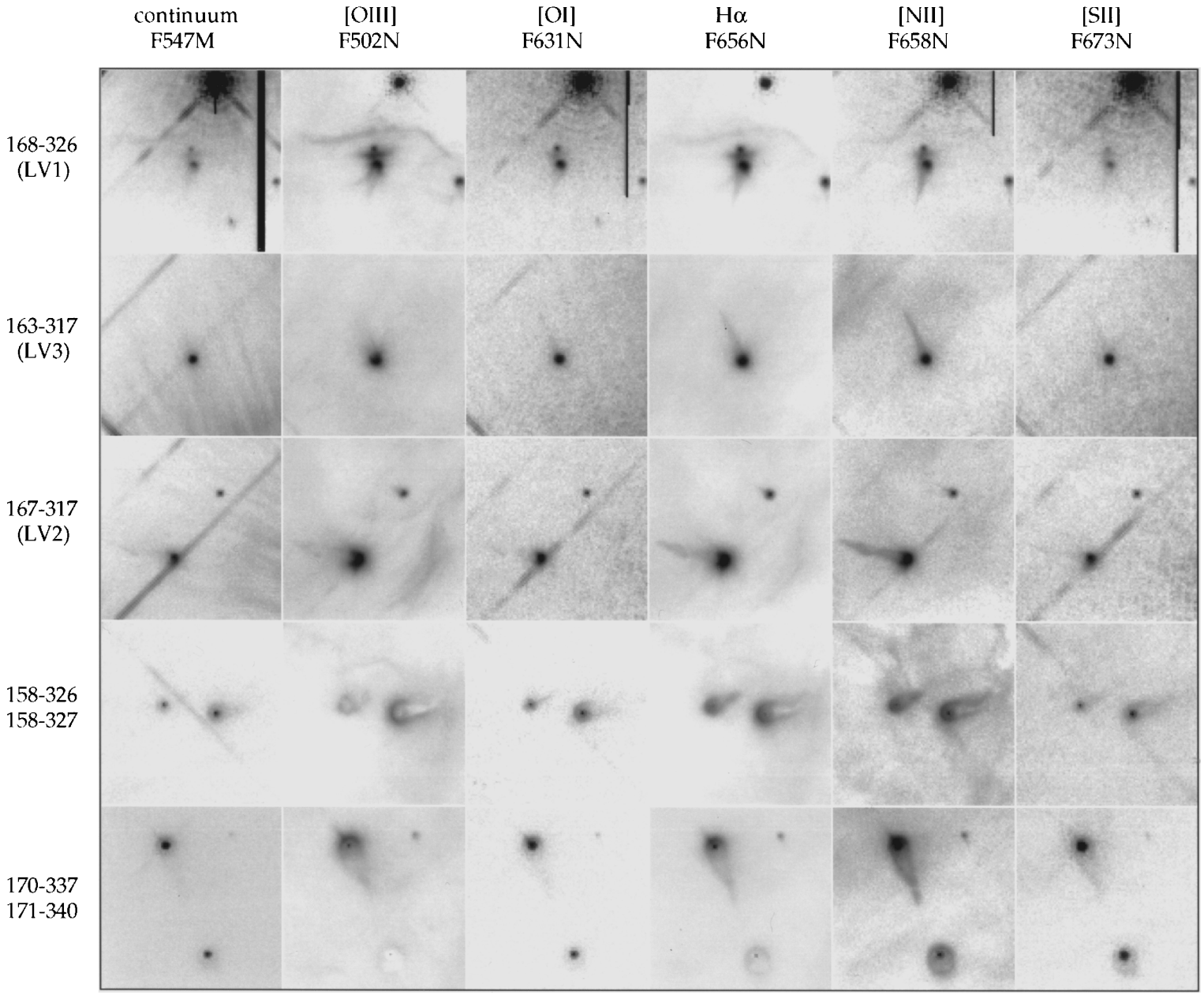

FIG. 7.—Mosaic of gray-scale images showing several externally illuminated YSOs in each of the observed filters. Each image is 100 × 100 pixels on a side, corresponding to an angular scale of 4.″55 or 1956 AU at the assumed distance of 430 pc in the PC. The eighth and tenth rows use WF data in which the 100 × 100 pixel field corresponds to 10″, or 4300 AU. The columns (*left to right*) show images in the continuum (F547M), [O III] (F502N), [O I] (F631N), Hα (F656N), [N II] (F658N), and [S II] (F673N). The rows show externally illuminated YSOs in order of increasing distance from θ^1 Ori C (*top to bottom*). Note the systematic variation of source properties with projected distance, such as the increased radii of the IFs, the disappearance of the [O III] + Hα arcs, the larger sizes of embedded silhouettes, and the disappearance of the IFs.

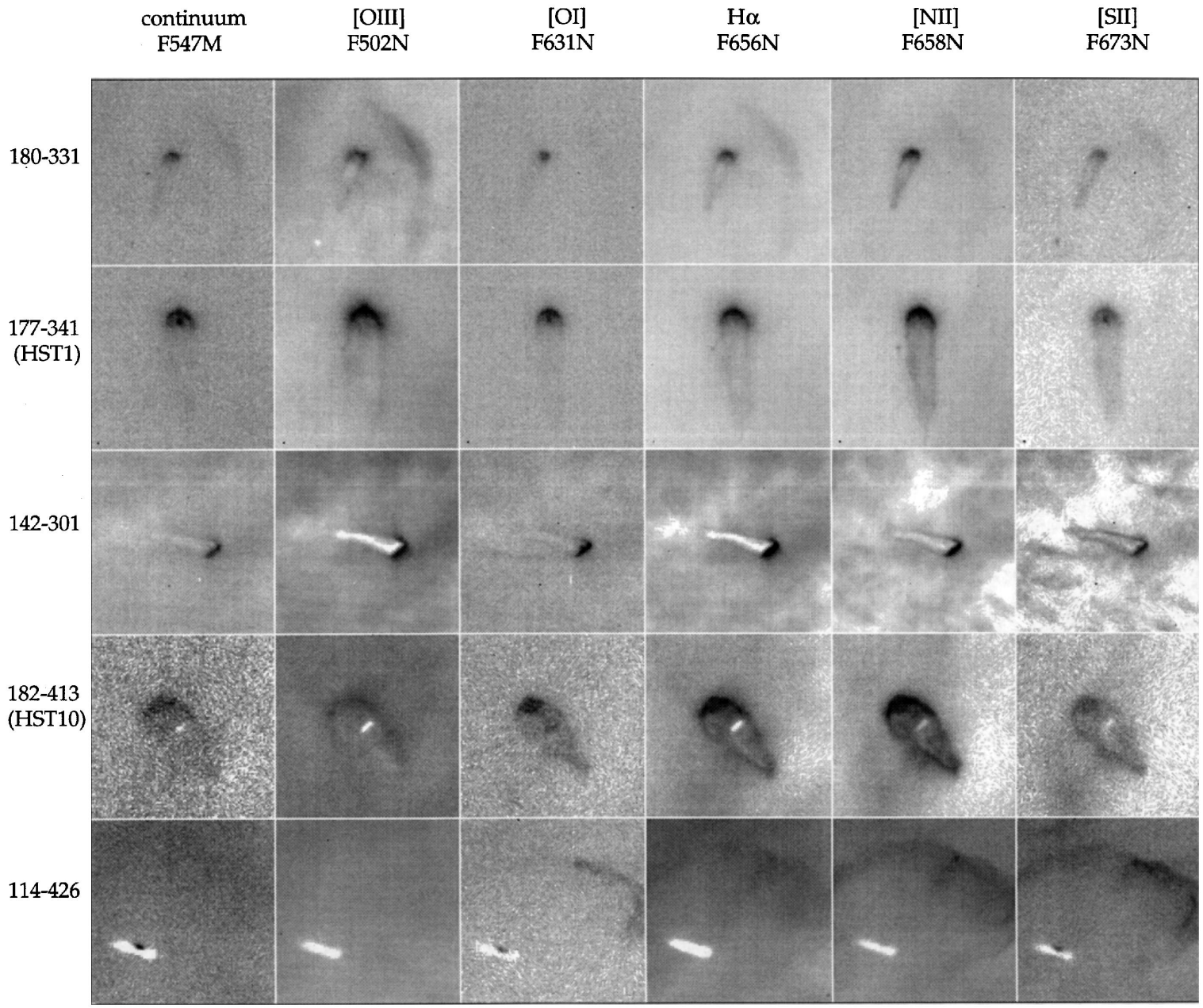

FIG. 7.—*Continued*

6. The source, 180−331 located at a projected distance of 16″.3 from θ^1 Ori C. The small pure silhouette 182−332 can be seen in the [O III] and Hα frames; 180−331 has a large [O III] + Hα arc that is slightly displaced to the right of the line pointing toward θ^1 Ori C.

7. The large object 177−341 (HST 1), located at a projected distance of 25″.6 from θ^1 Ori C. Note the faint companion to the lower left of the IF. This object has a large nearly 5″ radius [O III] + Hα arc that lies outside the field shown here but is visible in Figure 3. A faint silhouette can be discerned on the [O III] image in the center of the object.

8. (WF image). The object 142−301, at a projected distance of 40″.7 from θ^1 Ori C, has a flat head facing θ^1 Ori C. Note that the tail is seen in silhouette against background nebular light and is very opaque.

9. The teardrop-shaped object 182−413 (HST 10) is located at a projected distance of 57″ from θ^1 Ori C and contains an edge-on silhouette that is bright in [O I]. Also note the distinct [O I] emission component that coincides with the IF. Note that the axis of symmetry is nearly aligned with the minor axis of the silhouette and points about 20° due east of the line pointing to θ^1 Ori C.

10. (WF image). The giant silhouette 114−426 is located at a projected distance of 99″ from θ^1 Ori C. Note the large crescent of nebulosity to the upper right that is visible in [O I], Hα, [N II], and [S II] but not in [O III]. The crescent faces away from Trapezium, and its emission-line flux ratios are consistent with a low-excitation HH object (a shock-excited nebula powered by an outflow from a young star). The [N II] image shows a faint cone-shaped emission structure that connects the polar reflection nebula in the middle of the silhouette to the brightest portion of the crescent. It is possible that the [N II] structure traces a jet that powers the brightest portion of the crescent.

Figure 8 shows the FOC UV images of the field containing the sources LV 4, 5, and 6 (161−322, 158−323, and 158−327), as well as the sources 158−326 and 157−323. Unfortunately, this image was severely underexposed (even with a total 10 minute integration time), and we only present the image formed by summing all of the individual exposures. The individual externally illuminated YSOs are dominated by bright crescents on the side facing θ^1 Ori C, with fainter tails extending away from this star. The morphology is similar to that in the PC images. The central stars of several externally illuminated YSOs are easily seen in the UV images. In several objects, such as 158−326 and 158−327, the central stars are surrounded by symmetric silhouettes that appear darker than the general nebular background.

The pure silhouette 183−405 (HST 16) was also observed with FOC, though our image is severely underexposed and therefore not shown here. As in the visual-wavelength images, this YSO is surrounded by a symmetric and elliptical silhouette centered on a central star that is considerably fainter relative to the nebular background in the UV images. The shape and elliptically averaged surface brightness profiles of the silhouette are similar to those derived from the visual images. The main new result is that the silhouette appears to remain completely opaque as close to

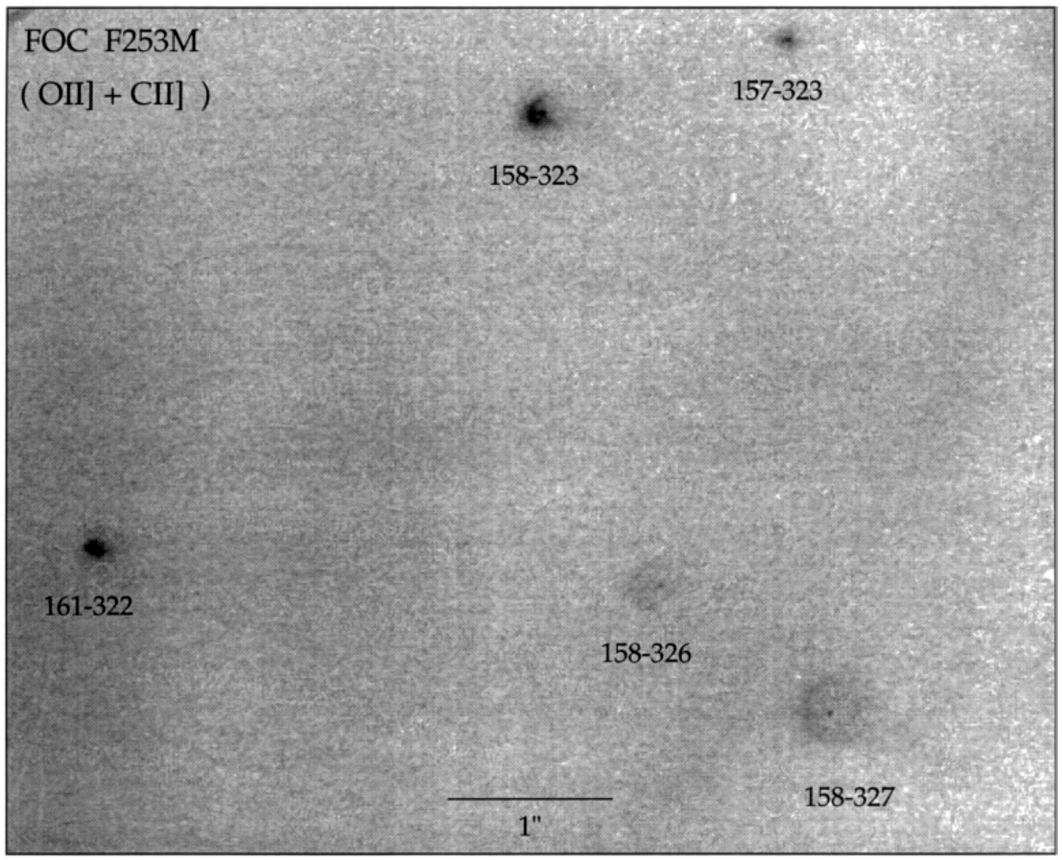

FIG. 8.—UV image of the field containing LV 4, 5, and 6 obtained with FOC. These images have a pixel scale of 9 AU, the highest linear resolution observations of a candidate protoplanetary disk obtained so far by any method. The orientation of these images is the same as in Figs. 3–6.

the central star as we can probe with FOC. Since the FOC is fully sampled and its point-spread function is about a factor of 2 smaller than that of the PC, and the central star is considerably fainter at UV wavelengths, we can trace the inner part of the silhouette to within about 0.″02 (10 AU) of the star.

3.3. *Observed Features of the Externally Illuminated YSOs*

In this section, we review the main observed features of externally illuminated YSOs within the Orion Nebula. In following sections, we discuss the interpretations of these features.

Figures 9 and 10 show two "cartoons" that illustrate the discussion. Figure 9 shows a schematic drawing of the Orion Nebula and its IFs, its stellar wind bubble and cavity, and several externally illuminated YSOs embedded within the various regions within the nebula. The features observed in an externally illuminated YSO depend on its location in the nebula. All externally illuminated YSOs *within* the nebula should be surrounded by IFs. Externally illuminated YSOs located *in front* of the nebula outside its Strömgren sphere (the "neutral lid"; O'Dell & Wen 1995) will lack an IF and can only be seen in silhouette if circumstellar dust is present. However, externally illuminated YSOs located inside the H II region sufficiently far from Trapezium may also be seen in silhouette if they have IFs that are fainter than the nebular background. The Hα + [O III] crescents discussed below are only seen close to Trapezium, and it is argued below that they trace interactions with the θ^1 Ori C stellar wind. Figure 10 is a schematic drawing of an externally illuminated YSO in the inner portion of the nebula showing the features discussed below.

3.3.1. *Emission-Line Crescents*

O'Dell & Wong (1996) catalog 153 YSOs in the Orion Nebula that are associated with extended structure. Six objects are seen in silhouette against the nebula (McCaughrean & O'Dell 1996) and are either completely dark or very faint in the observed emission lines. The rest are *bright* cometary objects whose extended structure is dominated by strong emission in Hα, [N II], [S II], [O I], and, to some extent, [O III]. On the side facing the principal ionization source, the projected shape of the brightest emission is well described by a half-circle or a crescent, suggesting that the emission region is hemispherical. The radii of the crescents range from 0.″05 (22 AU) for sources near θ^1 Ori C, such as 163−323 and 161−322, to over 2″ (860 AU) for the largest object, 252−457.

3.3.2. *Emission-Line Radial Intensity Gradients in the Crescents*

Figure 11 shows the azimuthally averaged and background-subtracted radial intensity profiles for a number of externally illuminated YSOs in the Hα line. Figure 12 shows a similar plot for the continuum. Table 3 lists the coordinates of all externally illuminated YSOs in the PC fields, as well as the larger and well-resolved objects that were imaged by the WF cameras of WFPC2. Table 4 lists the observed properties of these externally illuminated YSOs, including the dimensions of various emission and opaque components and the peak surface brightness of the objects in each emission line. For sources near θ^1 Ori C, the

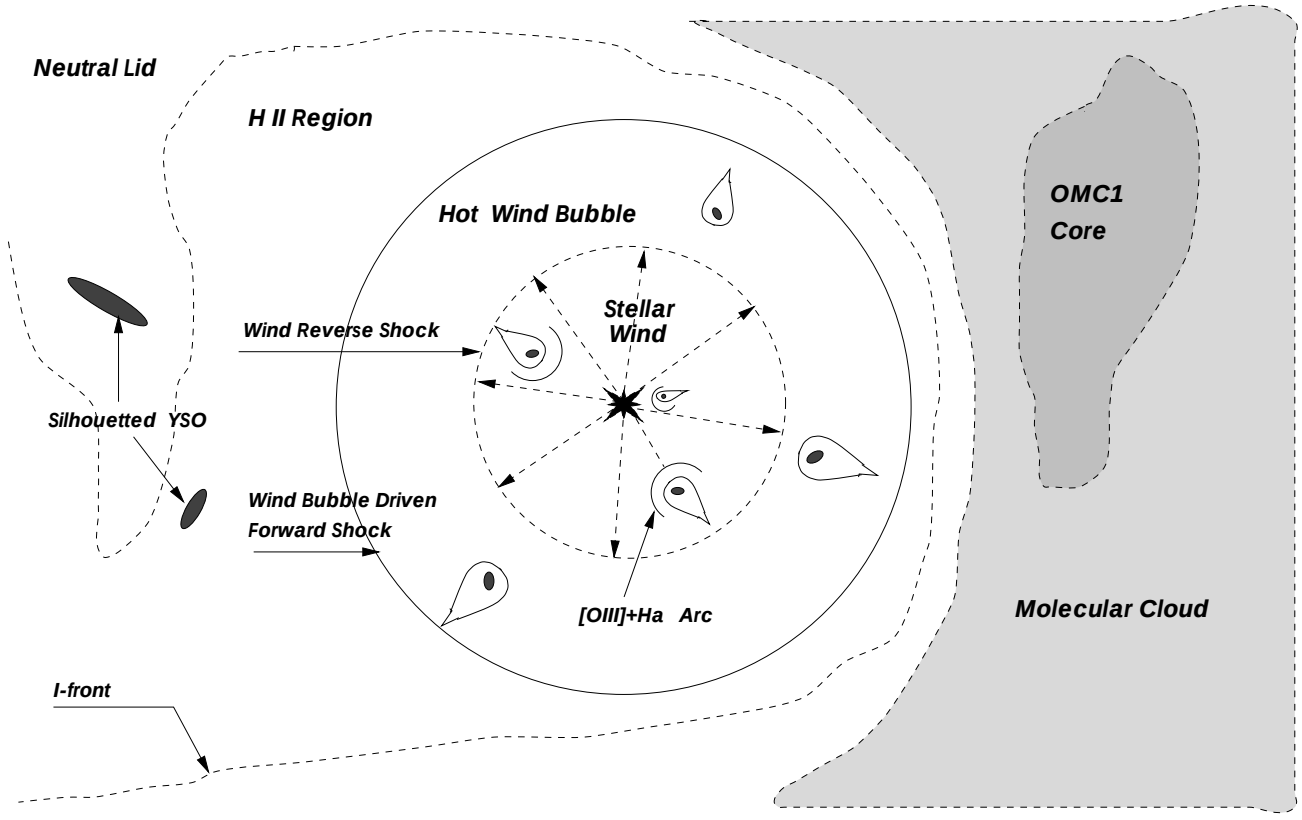

FIG. 9.—Schematic drawing of the Orion Nebula showing the θ^1 Ori C stellar wind bubble, the interface between the H II region and the background molecular cloud, the foreground "neutral lid," and externally illuminated YSOs embedded in various portions of the nebula. The line of sight to the Sun is toward the left.

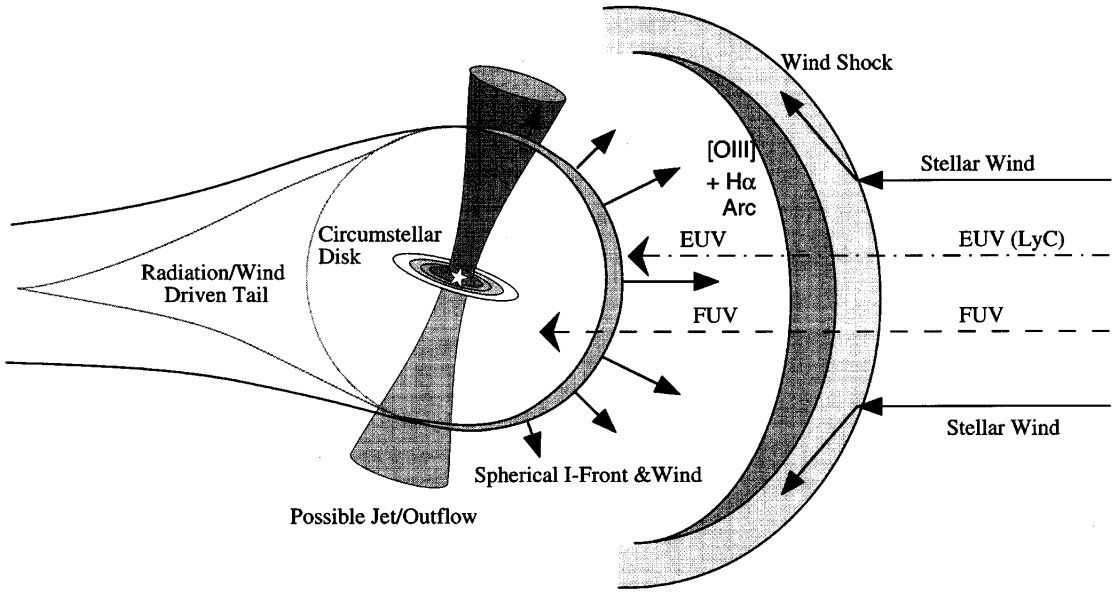

FIG. 10.—Schematic drawing showing an externally illuminated YSO. The young star has a circumstellar disk and a bipolar outflow or jet. FUV radiation ($2000 > \lambda > 912$ Å) shines on the circumstellar disk, initiating a low-velocity (≈ 3 km s^{-1}) disk wind (cf. Johnstone et al. 1998). At several disk radii, the quasi-spherical disk wind passes through a weak D-type IF and is accelerated to about 10 km s^{-1} greater than the sound speed in the ionized gas. The weak shock associated with this front lies just inside the IF and may produce and slight density and column density enhancement that is seen in silhouette in some objects. The electron density just outside the IF is about 10^5 cm^{-3} and is expected to decrease as r^{-2}, where r is the distance from the low-mass star, resulting in an r^{-3} decrease in surface brightness of emission lines. For externally illuminated YSOs embedded in the ram pressure–dominated portion of the θ^1 Ori C stellar wind cavity, a stationary bow shock forms where the ram pressures of the photoablation flow and the stellar wind are approximately equal, producing a region that is visible in Hα and [O III]. For externally illuminated YSOs embedded in the hot stellar wind bubble, the photoablation flow is subsonic and no shock can form. In this region, heat conduction gradually raises the temperature of the photoablation flow until it merges smoothly with the hot stellar wind bubble, and no Hα + [O III] arcs concentric with the IF are expected. The surface brightness of emission lines is expected to decrease exponentially with increasing distance from the source in this region.

radial profiles are well fitted over about 2 orders of magnitude in intensity by a power law of the form $r^{-\alpha}$, where $\alpha \sim 3$. However, for some objects an exponential profile of the form e^{-r/r_0} may yield a better fit with a length scale $r_0 \approx 7 \times 10^{14}$ cm (O'Dell 1998). There is a loose correlation between the cusp radius and the distance to θ^1 Ori C, with the cusp radius increasing as $r(d) \propto d^{\alpha}$ with $\alpha = 0.5$–0.8, where d is the projected distance from θ^1 Ori C. The peak surface brightness in each emission line decreases with increasing distance from θ^1 Ori C roughly as d^{-2}.

3.3.3. *Cometary Tails*

Most externally illuminated YSOs contain tails pointing directly away from the primary illuminator (either θ^1 Ori C, θ^1 Ori B, or θ^2 Ori A). Deviations between the tail axis and the line connecting the externally illuminated YSO to the main source of ionization are at most a few degrees. Some tails show irregularities, especially toward the tail tips. Parts of many tails are seen as silhouettes in [N II] and [O III], and to some extent in the other images, providing evidence for substantial amounts of dust in the tails. Externally illuminated YSOs at greater distances from θ^1 Ori C exhibit teardrop shapes with larger radius IFs facing the illuminating star. The tails are limb-brightened in the brighter emission lines and especially in [N II]. As shown in Table 4, the tails have lengths ranging from 0.″3 to nearly 4″. There is no correlation between tail length and the projected distance from the ionizing source. However, sources near θ^1 Ori C tend to have tails with large aspect ratios (ratio of length divided by the width), while objects at large projected distances tend to have stubby tails with relatively low aspect ratios. This follows from the observation that the tails always connect smoothly to the forward-facing emission-line crescents, which tend to have larger radii at larger projected distances from θ^1 Ori C.

3.3.4. *Silhouetted Disks Embedded in the Bright Externally Illuminated YSOs*

About 20% of the externally illuminated YSOs shown in Figure 7 contain dark and opaque cores seen in silhouette against the diffuse background light. The dark structures tend to be symmetric and centered on the embedded star (when the star is visible) and appear similar to the six silhouettes discussed by McCaughrean & O'Dell (1996). The pure silhouettes, however, are not surrounded by crescents or tails that emit in emission lines. The silhouettes found at the centers of the bright externally illuminated YSOs tend to be much smaller (by up to a factor of 20) than the pure silhouettes such as 114−426 or 183−405 and are most clearly seen in the larger objects that lie at relatively large projected distances from Trapezium. When both a silhouette and an emission-line crescent are seen, the ratio of the emission-line crescent radius divided by the semimajor axis of the silhouette ranges from about 1.5 to 4.

Most objects within 20″ of θ^1 Ori C are so compact that no central opaque regions are seen in the PC image. Dark cores may be hidden by the combined light of the nebular lines and the embedded star. However, in the shorter wavelength UV images obtained with FOC, evidence for a compact dark zone surrounding the central stars is clearly seen. Figure 8 shows a UV image of five objects located roughly 10″ west of θ^1 Ori C at a wavelength of 2530 Å taken with FOC. Cometary tails point directly away from θ^1 Ori C, which is located to the left. In the FOC image, all

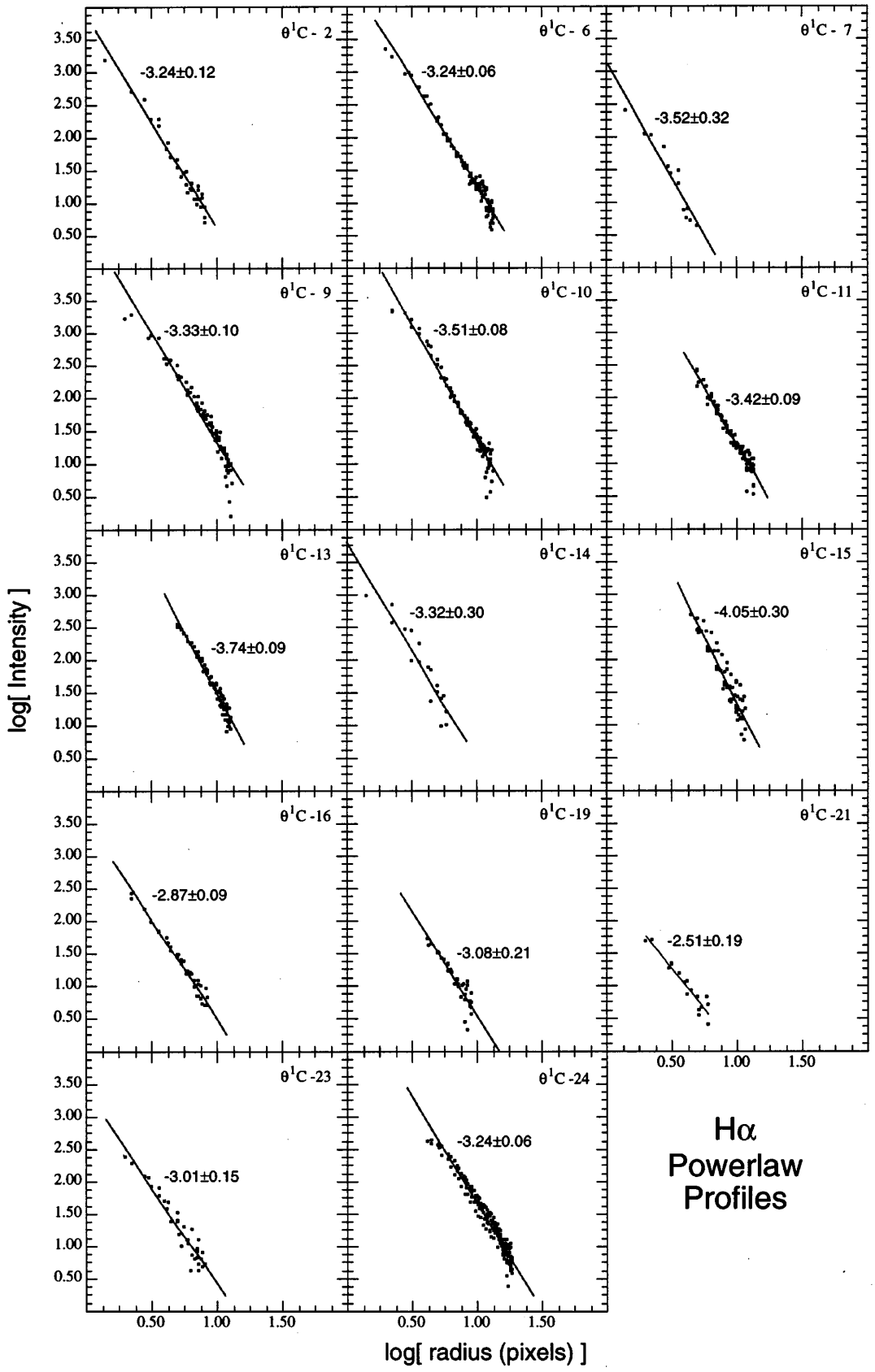

FIG. 11.—Azimuthally averaged background-subtracted radial intensity profiles for 14 externally illuminated YSOs in the Hα line. This diagram shows the data on a log-log plot along with the best-fit power law that describes the correlation. The power-law index and formal uncertainty are shown.

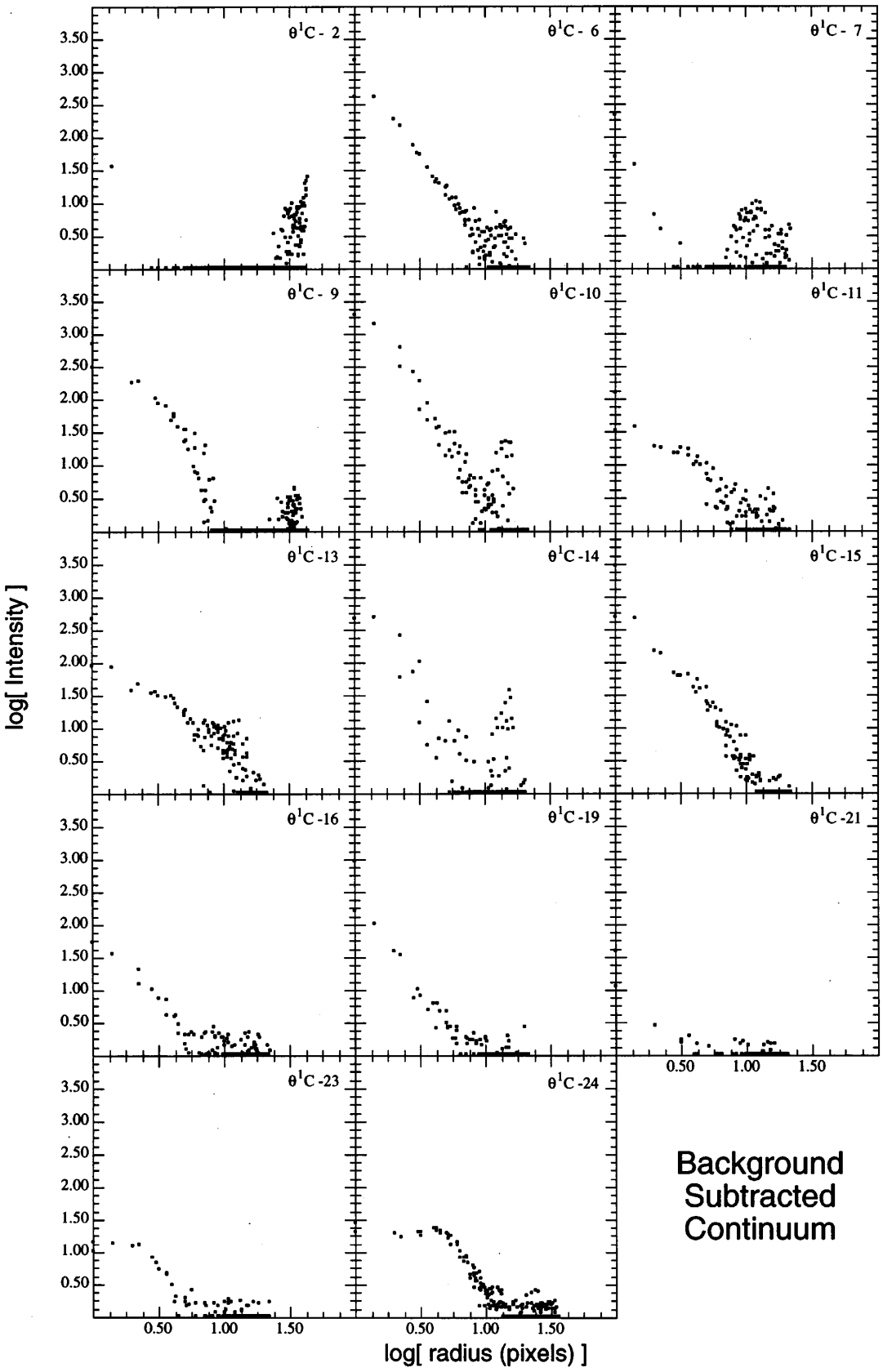

FIG. 12.—Azimuthally averaged background-subtracted radial intensity profiles for 14 externally illuminated YSOs in the continuum

TABLE 3

POSITIONS OF TRAPEZIUM STAR-DISK SYSTEMS

Number[a]	Star	α (J2000.0) (05^h35^m)	δ (J2000.0) ($-05°$)	Frame[b]	X (pixels)	Y (pixels)	OW[c]	Comments
1.....	θ^1 C	16.286	23 23.14	LV 3 (1)	327	521	163−323	In glare of θ^1C
2.....	θ^1 C	16.026	23 24.80	LV 3 (1)	240	487	161−322	LV 4
3.....	θ^1 C	16.788	23 26.45	LV 3 (1)	394	690	168−326	LV 1, fainter of two sources
4.....	θ^1 C	16.801	23 26.77	LV 3 (1)	392	698	...	LV 1, brighter of two sources
5.....	θ^1 C	16.718	23 28.54	LV 3 (1)	345	707	168−328	
6.....	θ^1 C	16.245	23 17.08	LV 3 (1)	411	416	163−317	LV 3
7.....	θ^1 C	16.573	23 16.65	LV 3 (1)	495	485	166−316	
8.....	θ^1 B	16.062	23 14.75	LV 3 (1)	404	337	161−314	Faces θ^1 B
9.....	θ^1 C	16.037	23 28.31	LV 3 (1)	188	545	161−328	Disk in [O I]
10	θ^1 C	16.703	23 16.95	LV 3 (1)	521	520	167−317	LV 2, tail kinks, multiple arcs
11	θ^1 C	15.796	23 22.98	LV 3 (1)	214	405	158−323	LV 5
12	θ^1 C	15.805	23 26.01	LV 3 (1)	169	455	158−326	
13	θ^1 C	15.753	23 27.08	LV 3 (1)	140	460	158−327	LV 6, disk in [O I]
14	θ^1 C	15.691	23 23.00	LV 3 (1)	189	381	157−323	
15	θ^1 C	16.934	23 37.71	HST 1 (1)	294	204	170−337	Jet, [O I] disk
16	θ^1 C	17.507	23 25.55	HST 1 (1)	618	145	176−325	
17	θ^1 C	16.844	23 38.66	HST 1 (1)	258	198	169−338	
18	θ^1 C	16.020	23 28.38	HST 3 (1)	776	94	160−328	Disk in [O I]
19	θ^1 C	15.321	23 24.55	LV 3 (1)	77	320	154−324	
20	θ^1 C	15.822	23 38.73	HST 3 (1)	576.2	213.7	159−338	
21	θ^1 C	17.012	23 40.37	HST 1 (1)	271	264	171−340	End-on?
22	θ^1 C	15.175	23 19.30	LV 3 (1)	124	203	152−319	Silhouette in [O III]
23	θ^1 C	15.442	23 38.20	HST 3 (1)	495.0	117.2	155−338	
24	θ^1 C	17.279	23 41.97	HST 1 (1)	309	351	173−341	
25	θ^1 C	17.992	23 31.45	HST 1 (1)	640	351	180−331	[O III] + Hα arc one-sided
26	θ^1 C	17.628	23 41.59	HST 1 (1)	397	426	177−341	HST 1
27	θ^1 C	18.141	23 32.17	HST 1 (1)	664	397	182−332	Silhouette
28	θ^1 C	15.889	23 50.32	HST 3 (1)	412.5	412.3	159−350	Faint companion to HST 3
29	θ^1 C	15.867	23 50.73	HST 3 (1)	410.9	413.7	159−350	HST 3
30	θ^1 C	15.916	23 53.68	HST 3 (1)	366.9	471.3	160−353	Cloverleaf-shaped IF
31	θ^1 C	16.923	22 49.40	HST 1 (4)	327	502	170−249	
32	θ^1 C	17.493	23 55.61	HST 1 (1)	147	616	175−355	
33	θ^1 C	17.913	23 54.06	HST 1 (1)	270	689	...	
34	θ^1 C	14.140	23 01.27	HST 1 (4)	534	117	142−301	[O I] disk
35	θ^1 C	15.345	22 40.82	HST 1 (4)	555	392	154−240	
36	θ^1 C	16.432	22 36.49	HST 1 (4)	472	540	165−235	Bipolar jet source?
37	θ^1 C	18.273	24 05.04	HST 10 (1)	561	323	183−405	HST 16 silhouette
38	θ^1 C	17.444	22 34.62	HST 1 (4)	379	633	173−236	
39	θ^1 C	17.341	24 14.50	HST 10 (1)	202	249	174−414	
40	θ^1 C	18.161	24 14.18	HST 10 (1)	400	434	182−413	HST 10, central star not visible
41	θ^2 A	18.250	24 19.48	HST 10 (1)	339	538	183−419	Faces θ^2 A, central star not visible
42	θ^1 C	18.297	24 27.38	HST 10 (1)	227	674	184−427	[O I] disk
43	θ^1 C	11.288	24 26.86	HST 10 (3)	698	511	114−426	Giant silhouette, central star not visible

NOTE.—Units of right ascension are seconds, and units of declination are arcminutes and arcseconds.

[a] Labels used to identify objects in Figs. 11 and 12.

[b] Numbers in parentheses indicate which WFPC2 CCD was used: (1) is the PC and (2), (3), and (4) refer to one of the three available WFs.

[c] Designation given in O'Dell & Wong 1996.

five objects show unresolved stellar images at the centers of the cometary condensations. Two objects show dark regions inside the crescent-shaped bright rims that are symmetric about the central stars.

3.3.5. [O I] *Emission from Silhouettes Embedded in Bright Objects*

Some dark silhouettes (dark in [O III], [N II], [S II], or Hα) embedded inside the bright, externally illuminated YSOs surrounded by emission-line crescents are *bright* in the [O I] images. The spatial extent, orientation, and structure of the [O I] emission matches those of the dark silhouettes. However, in the six pure silhouettes (YSO disks seen only in silhouette that are not surrounded emission-line regions), the disks are also dark in [O I]. The large teardrop-shaped object 182−413 (HST 10) has several extended [O I] emission components. The central region is seen as a prominent elongated silhouette in ionized species ([S II], [N II], and [O III]) and in Hα. However, this region is *bright* in the [O I] image. The teardrop-shaped outer boundary that is bright in Hα and in the ions is also bright in [O I]. Finally, there is diffuse [O I] emission in the entire projected interior of 182−413 that is several times fainter than the emission produced by the silhouette or the outer boundary.

3.3.6. *Central Stars*

The F547M continuum images show the presence of central stars in about 80% of the externally illuminated YSOs. Infrared images show that all except a few notable objects (cf. 114−426 and 182−413) contain central stars. These stars are centered with respect to hemispherical IFs facing the dominant illuminating UV source. The few objects in which no central stars have yet been directly seen contain highly elongated silhouettes at their centers. The absence of stars in these objects sets a minimum limit on the column density along the line of sight. As discussed by Chen et al. (1998), the failure to detect a central star in 182−413 implies a minimum visual extinction of 50 mag, or a column density of order $N(\mathrm{H}) = 10^{23}$ cm^{-2}. Dividing the column density by the major semidiameter of the silhouette (0.″175,

TABLE 4

PARAMETERS FOR TRAPEZIUM STAR-DISK SYSTEMS

Number	D_* (arcsec)	$R_{I,\perp}$ (arcsec)	$R_{I,\parallel}$ (arcsec)	$r_{D,\perp}$ (arcsec)	$r_{D,\parallel}$ (arcsec)	L(tail) (arcsec)	r([O III]) (arcsec)	I(Hα)[a,b]	I([N II])[a,b]	I([S II])[a]	I([O III])[a,b]	I_d([O I])[a,c]	I_{IF}([O I])[a,c,d]	Features[e]
1	2.08	0.08	<0.08	...	...	...	...	2390	<200U	<200U	1880	U	<200U	T, *
2	6.09	0.08	<0.05	...	...	1	1.2	1726	83	<24U	1140	U	<54U	T, *, O
3	6.19	<0.05	...	...	...	...	0.55	1040	46	<9U	658	U	<40U	T, *, O
4	6.54	0.1	<0.1	...	...	1.05	0.95	1900	94	<29U	1560	U	<67U	T, *, O
5	6.71	<0.05	<0.05	...	...	0.7	1.0	915	51	<26U	719	U	<16U	T, *, O
6	6.93	<0.1	0.1	...	...	1.6	2.6	2191	<76	<302U	1581	U	<230U	T, *
7	7.19	<0.05	...	<0.045	...	0.4	0.75	729	49	<61U	513	U	<16U	T, *, O
8	7.50	0.1	...	...	...	0.3	...	91	19	<29U	15	U	<4	t, *
9	7.53	0.15	0.05	0.09	...	0.4	...	153	21	1.5	56	7.7	6.6	t, *, S, o
10	7.76	0.15	<0.1	...	...	2.1	2.1	2731	119	<147U	1890	U	<42	T, *, O
11	9.36	0.1	0.08	...	...	1.8–2.5	...	1636	69	<687U	1156	U	35	T, *, O
12	9.57	0.2	0.2	0.09	0.045	0.85	...	252	36	3.1	81	U	<12	T, *, S
13	10.64	0.25	0.25	0.045	...	1.0–1.5	...	327	42	8.0	227	15	11	T, *, S, o
14	10.95	0.08	<0.05	...	...	<0.7	...	654	33	424U	237	U	<58	T, *, O
15	16.14	0.25	0.2	0.09	...	1.75	...	629	79	5.2	234	<39	11	T, *
16	16.31	0.15	<0.1	...	...	1	...	624	77	5.6	321	<17	<11	T, *
17	16.43	<0.05	<0.05	...	...	0.4	...	146	17	<2	50	U	2U	T, *
18	16.5	0.08	0.15	0.1	0.045	0.5	...	162	24	5.0	55	8.3	4.3	t, *, o
19	16.51	<0.05	<0.05	...	...	0.3	...	226	19	<2	120	U	4U	T, *
20	17.70	0.08	0.08	<0.045	<0.05	0.8	...	413	49	5.8	185	U	1U	T, *
21	19.04	0.25	0.15	0.09	0.09	0.7	...	55	17	2.9	17	9	1	t, *, S
22	19.09	0.25	0.15	0.09	<0.08	<0.5	...	65	15	<5.8	15	U	5U	t, *, S
23	20.80	0.20	0.20	0.09	0.05	1.5	...	203	58	5.9	117	12	14	T, *, S
24	22.49	0.1	0.1	<0.045	...	0.7	...	<186	<43	<4.1	<42	U	<7U	T, *
25	24.75	0.2	<0.15	...	...	1.5	1.5	232	47	3.3	95	4	4	T, *, O
26	25.55	0.35	0.3	<0.18	<0.09	3.5	4.0	372	71	6.3	176	4.4	7	T, *, O, S, o
27	27.09	...	...	0.1	0.045	...	...	−11	...	...	−20	...	...	*, S
28	27.99	<0.1	<0.1	<0.05	<0.05	...	...	171	<61	<3	76	U	<8	*
29	28.49	0.30	0.35	<0.1	<0.09	1.7	...	362	94	<8	158	U	<8	T, *
30	31.14	0.30	0.30	<0.05	<0.05	0.6	...	111	28	<6	35	U	7	t, *
31	34.89	0.3	0.3	...	...	2.0	...	146	46	2.6	51	2.6	2.1W	T, *
32	35.89	0.15	0.15	0.09	0.09	...	...	14	4.4	<1.7	−5.6	3.3	...	t, *, S
33	37.82	<0.05	<0.05	...	...	0.6	...	29	10	<1	−5.6	1.1	...	T, *
34	40.70	0.4	<0.2	0.25	<0.09	2.0	...	293	76	4.1	99	1.9	5.4W	T, S, o
35	45.60	0.3	0.2	0.09	0.045	0.9–1.7	...	56	23	1.3	7	1.0	1.0W	T, *, S, o
36	46.99	...	...	...	...	...	...	37.5	13.8	3.2	6.9	<2	2.4W	t, *
37	50.27	...	...	0.45	0.3	...	...	−38	−6.2	−1.0	−3.2	<1	...	*, S
38	51.19	0.3	0.3	...	...	3.0	...	169	42	<1.0	46	U	4W	T, *
39	52.82	0.1	0.1	...	...	0.5	...	31	11	<2.0	−5.6	U	<4.4	T, *
40	56.95	0.5	0.7–1.0	0.18	0.09	1.75	...	79	28	2.4	18	1.7	2.2	t, S, o
41	61.0	0.35	0.4	0.15	<0.08	...	...	29	11	3.2	−21	1.7	1.2	t, S, o
42	69.77	0.15	0.1	<0.05	<0.05	1	...	49	15	<1.0	8.3	1	1.7	T, *, S, o
43	99.48	...	...	1.2	0.1	...	...	−14.5	−2.6	...	−11.7	0	0	S

[a] Units are in 10^{-16} ergs cm^{-2} s^{-1} in a PC pixel, which is a square 0.″0455 on each side.

[b] A minus sign in front of a flux implies that it is seen in silhouette.

[c] The column labeled I_d([O I]) refers to the component of the [O I] emission originating in the silhouetted feature or circumstellar disk. The column labeled I_{IF}([O I]) refers to the component of the [O I] emission associated with the IF. A "U" indicates that the IF and disk are unresolved.

[d] A "W" indicates images in the WF CCD only, which has a pixel scale of 0.″1. The quoted surface brightness has been scaled to the PC pixels by multiplying the observed flux in the WF pixels by 0.207.

[e] (T) tail; (t) very stubby or teardrop-shaped tail; (*) central star; (O) [O III] + Hα arc; (S) circumstellar silhouette; (o) extended [O I] emission from silhouette.

or 75 AU) implies a minimum mean density of about 10^8 cm^{-3} for the silhouette in 182−413.

3.3.7. [O III] + Hα *Arcs*

Within 30″ of θ^1 Ori C, the *HST* observations show arcs of [O III] + Hα emission centered on the proplyds and concentric with the Hα-dominated emission-line crescents. Examples include LV 1 (168−326), LV 2 (167−317), and LV 4 (161−322) in Figure 2 and the objects 168−326, 167−317, and 180−331 in Figure 7. The source 177−341 has such an arc (Fig. 3). Massey & Meaburn (1995) and Hu (1996) obtained long-slit spectra of several of these objects, and O'Dell et al. (1997) measured their radial velocities with a Fabry-Perot interferometer. The Hα + [O III] arcs near Trapezium all appear to be redshifted, with velocities ranging up to about 100 km s^{-1}. The nearly edge-on disk seen in silhouette as 114−426 (Fig. 7, *bottom*) is surrounded by a low-excitation arc bright in [O I], [N II], and [S II]. Unlike the Hα + [O III] arcs surrounding the other proplyds, this arc faces *away* from Trapezium and may be shock-excited by a wind blowing from the central star embedded within the silhouette. The [O III] + Hα arcs are located between the proplyds and θ^1 Ori C about 0.″5 to 4″ from their IFs with radii of curvature about 3 to 10 times larger than the radii of these fronts. The ratio of the projected distance between the proplyd and the arc divided by the projected distance between the arc and θ^1 Ori C ranges from 0.05 to 0.2. These arcs are only visible in the Hα and [O III] images and are high-excitation features. Their surface brightness is comparable to that of the nebula, which implies that the product of the square of their densities and the observed path through them is comparable to the emission measure of M42, where this product is about 10^6 cm^{-6} pc. Since the observed path length is probably comparable to about half of their observed sizes of 4″ (i.e., their lengths are about 0.004 pc), their densities must be about 1.5×10^4 cm^{-3}.

A second family of [O III] + Hα arcs appears not to be associated with stellar objects. These objects appear to have random orientations with respect to θ^1 Ori C, and many exhibit large radial velocities (O'Dell et al. 1997; Meaburn 1986, 1988). Both types of arcs have shapes reminiscent of bow shocks.

4. INTERPRETATION

The observed properties of the externally illuminated YSOs reflect the evolutionary status of the YSOs and interactions with radiation and massive star winds in the Orion Nebula. We review the environment of the Orion Nebula and discuss the role that various physical processes play in determining the appearance of young stars embedded within it.

The region surrounding the Trapezium stars contains a stellar wind bubble created by the wind from θ^1 Ori C, a photoionized zone dominated by Lyman continuum radiation, and a predominantly neutral layer that separates the H II region from the molecular cloud that lies in the background. Observations show that there is also a layer of neutral gas in front of the nebula, the so-called neutral lid (O'Dell & Wen 1995). Figure 9 shows a schematic drawing of the Orion Nebula, illustrating the various features discussed below, and Figure 10 shows a schematic drawing of an externally illuminated YSO. The various features shown in this drawing are discussed below, starting with the features most distant from the YSO.

4.1. *The θ^1 Ori C Stellar Wind and Its Bubble*

θ^1 Ori C has a strong stellar wind, with $\dot{M}_w \approx 4 \times 10^{-7}$ $M_\odot$ yr^{-1} at a velocity of $v_w \approx 10^3$ km s^{-1} (Howarth & Prinja 1989), which drives a bubble into the surrounding medium. A stellar wind bubble contains two zones (Weaver et al. 1977; Castor, McCray, & Weaver 1975). The inner region is dominated by the ram pressure of the wind,

$$\frac{P_{\rm ram}}{k} \approx \frac{\rho_w v_w^2}{k} = \frac{\dot{M}_w v_w}{4\pi k d^2} \approx 4 \times 10^7 \dot{M}_{-7} v_3 d_{17}^{-2} \text{ cm}^{-3} \text{ K}, \quad (2)$$

where $\dot{M}_{-7}$ is the stellar wind mass-loss rate in units of 10^{-7} $M_\odot$ yr^{-1}, v_3 is the wind velocity in 10^3 km s^{-1}, and d_{17} is the distance from θ^1 Ori C in units of 10^{17} cm. The wind passes through a reverse shock at $R_s = 3 \times 10^{17} \dot{M}_{-7}^{3/10} n_3^{-3/10} v_3^{1/10} t_5^{2/5}$ cm, where n_3 is the undisturbed gas density outside the wind bubble in units of 10^3 cm^{-3} and t_5 is the age of the bubble in units of 10^5 yr. This region is surrounded by a hot ($>10^6$ K) bubble of shocked wind material dominated by thermal pressure. The expansion of this bubble drives a forward shock into the surrounding medium at a radius $R_{\rm fs} = 3 \times 10^{18} \dot{M}_{-7}^{1/5} n_3^{-1/5} v_3^{2/5} t_5^{3/5}$ cm and velocity $v_{\rm fs} = 6.0 M_{-7}^{1/5} n_3^{-1/5} v_3^{2/5} t_5^{-2/5}$ km s^{-1}.

An extended, high-velocity, blueshifted [O III] feature has been found south of Trapezium in Fabry-Perot data cubes of the Orion Nebula, which may trace the forward shock of the θ^1 Ori C stellar wind bubble (O'Dell et al. 1997). In addition, high-dispersion long-slit spectra show an extended blueshifted [O III] feature north of Trapezium (Massey & Meaburn 1993) that may also trace parts of this shock. This component of the [O III] emission has been traced to about 60″ to 100″ (0.1 to 0.2 pc) from Trapezium and has velocities of up to about −90 km s^{-1} with respect to the nebular emission. As discussed by O'Dell et al. (1997), the dynamic age of this feature is very short, less than 5000 yr.

A condensation such as an externally illuminated YSO lying within the wind bubble will present an obstacle to the expanding wind. In the ram pressure–dominated interior portion of the wind bubble, the stellar wind will pass through a stationary bow shock that wraps around the obstacle. The location of this shock is determined by the balance between the wind ram pressure and the pressure presented by the obstacle. As we argue below, the obstacle pressure is dominated by the photoablation flow from the YSO environment.

In addition to the extended high-velocity gas, localized high-velocity features have been known to exist in the core of the Orion Nebula for some time. Some are HH objects powered by young stars still deeply embedded within the dense cloud behind the nebula (Taylor & Münch 1978; Axon & Taylor 1984; Meaburn 1986). Others are associated with the brightest externally illuminated young stars within the nebula, the Laques & Vidal (1979) LV sources (Meaburn 1988; Meaburn et al. 1993). While most HH objects are blueshifted, the high-velocity emission associated with the LV sources are predominantly redshifted by over 100 km s^{-1} and most readily visible in [O III] spectra and images. The brightest externally illuminated YSOs in

the immediate vicinity of Trapezium (LV 1, 2, 3, 5, and 6) are associated with high-velocity redshifted [O III] emission. Our images show a nearly one-to-one correspondence between the location of this high-velocity gas and the presence of [O III] + Hα arcs, and it is therefore tempting to associate these two phenomena. Below, we explore this possible connection further.

Henney et al. (1996) argue that the θ^1 Ori C stellar wind reaches the surfaces of disks surrounding YSOs embedded in the nebula and is responsible for the emission-line structure. However, Johnstone, Hollenbach, & Bally (1998) have shown that, in the presence of Lyman continuum and far-UV (FUV) radiation with wavelengths longer than 912 Å, a layer of photoheated material insulates the disk from the wind. The expansion of this neutral layer drives the IF away from the disk surface. Divergence of this flow allows Lyman continuum radiation to penetrate the outer portions of this flow to establish a roughly hemispherical IF at a distance of several disk radii. The relative line strengths, radial emissivity profiles, and morphologies indicate that the bright emission-line crescents surrounding the YSOs embedded in the Orion Nebula are IFs propagating into the soft-UV–powered wind expanding away from a dense circumstellar reservoir such as a disk. Once photoionized, the wind accelerates to about the sound speed in ionized gas and continues to expand until its ram pressure drops to that of the stellar wind blowing from θ^1 Ori C, the thermal pressure of the surrounding wind bubble, or the pressure of the H II region.

Some YSOs may be embedded in the hot 10^6 K wind bubble beyond the ram pressure–dominated part of the wind. In this post–wind-shock region (outside the reverse shock), the local sound speed is higher than the bulk velocity of the outward-moving plasma. This stellar wind plasma flows past stationary obstacles at roughly the velocity of the forward shock driven into the surrounding H II region by the expansion of the wind bubble. Thus, the flow of the stellar wind bubble around a YSO and its circumstellar environment is subsonic, and a wind shock will not form.

4.2. *Ionization Fronts Associated with the Externally Illuminated YSOs*

UV radiation interacts with the YSO environment by dissociating molecules, heating and ionizing the gas, and through radiation pressure acting on dust. The Trapezium cluster has a total luminosity of about $10^5\ L_\odot$, and θ^1 Ori C has a Lyman continuum luminosity of about $Q = 1.5 \times 10^{49}$ photons s^{-1} ($L_{\rm Lyc} \approx 8 \times 10^4\ L_\odot$). Consider a static, spherical condensation in the path of the advancing IF. The advancing front will be retarded as it enters the region of higher density because of the increased recombination rate in the higher density medium. For a D-type IF advancing subsonically into the medium, the total recombination rate between the star and the IF is balanced by the photoionization rate produced by the incident flux, $F_{\rm Lyc} = Q/4\pi d^2$, where d is the distance from θ^1 Ori C.

The Hα-dominated emission-line crescents in the externally illuminated YSOs have typical radii of order 25 to 500 AU. The emission-line flux ratios derived from the peak surface brightness of various emission lines given in Table 4 are consistent with emission produced by a photoionized plasma (cf. Sutherland 1997). If we assume that the crescents trace the IFs at the surface of a spherical cloud and also ignore the absorption by dust in the nebula, the electron density at the IF is expected to be approximately $n \approx (F_{\rm Lyc}/\alpha_B L)^{1/2} \approx 7 \times 10^5 L_{15}^{-1/2} d_{17}^{-1}$ cm^{-3}, where L_{15} is the characteristic radius of the IF in units of 10^{15} cm, d_{17} is the distance to the illuminating source in units of 10^{17} cm, and $\alpha_B \approx 2.6 \times 10^{-13}$ cm^3 s^{-1} is the case B recombination coefficient for hydrogen.

The electron density of the plasma just outside the externally illuminated YSO IF is one of the few physical parameters that can be determined with a fair amount of certainty. The electron density has been estimated by three methods: from the radio continuum (Felli et al. 1993a, 1993b), from the brightness of the Hα emission (corrected for extinction by the mean A_V to the Orion Nebula), and by fitting the observed intensities of trace ions and atoms in the IF using MAPPINGS2 (cf. Sutherland et al. 1993; Sutherland 1997). All methods yield electron densities at the IF that range from $n_e = 10^5$ to 10^6 cm^{-3}.

Most externally illuminated YSO crescents have peak surface brightnesses about 2–20 times brighter than the background nebula (see Table 4). The central density in the Orion Nebula is about 8000 cm^{-3} (Pogge et al. 1992), and the emitting line-of-sight path is about 0.13 pc (O'Dell & Wen 1995). Thus, if a typical externally illuminated YSO IF has a radius $L_{15} = 10^{15}$ cm ≈ 0.0003 pc (67 AU), the density required to produce a surface brightness 10 times higher than that of the central part of the nebula is $\langle n_e \rangle = 8000 (F_{\rm YSO}/F_{\rm M42})^{1/2} (0.13_{\rm pc}/L_{\rm pc})^{1/2} = 5 \times 10^5 L_{15}^{-1/2}$ cm^{-3}, which is in excellent agreement with the predictions for an IF.

The pressure of plasma at the IF is about $P_I/k \approx nT = 10^9 n_5\, T_4$ cm^{-3} K. The plasma thermal pressure is comparable to the radiation pressure acting on grains (total luminosity) and neutrals (Lyman continuum luminosity), which is of order $P_{\rm rad} = L/(4\pi c d^2) = 7.7 \times 10^8 L_5\, d_{17}^{-2}$ cm^{-3} K. For most externally illuminated YSOs, the thermal pressure at the IF is greater than the ram pressure of the θ^1 Ori C stellar wind. The pressure ratio is given by

$$\frac{P_I}{P_w} = \frac{\mu m_{\rm H} c_{\rm II}^2 d}{\dot{M}_w v_w} \left(\frac{4\pi Q}{\alpha_B L}\right)^{1/2} = 113 d_{17}\, \dot{M}_{-7}^{-1} v_3^{-1} Q_{49}^{1/2} L_{15}^{-1/2}\ .$$

Since this ratio is greater than unity, the stellar wind cannot reach the IF. Photoionized plasma will expand outward from the IF, forming a diverging wind at about the sound speed in ionized gas.

To first order, the flow from the IF is isothermal and spherical (at least in the hemisphere facing the illuminating star) and has a constant velocity at about the sound speed in ionized gas, $c_{\rm II} \approx 10$ km s^{-1}. The mass-loss rate through the IF is $\dot{M}_e \approx 2\pi\mu m_{\rm H} c_{\rm II} n_e L^2$, and the electron density outside the IF decreases as $n_e(r > L) = \dot{M}_e/4\pi\mu m_{\rm H} r^2 c_{\rm II}$, where r is the distance from the central low-mass star (or point of symmetry for a spherically divergent flow). The mass-loss rate from typical externally illuminated YSOs is about $10^{-7}\ M_\odot$ yr^{-1}. McCullough et al. (1995) show that the IF radii scale as $L \propto d^{2/3}$, which is consistent with the results shown in Table 4 and with a constant mass-loss rate approximately independent of the projected distance from the illuminating source. The ionized gas flowing away from the IF forms a low-velocity "IF wind" with a slightly steeper than r^{-2} density profile because of the slight acceleration of the flow by the radial pressure gradient.

The surface brightness at some projected radius from the IF is proportional to the emission measure, EM $\sim n_e^2\, l$, where l is the path length through the emitting region. For a spherical wind, the surface brightness is proportional to EM $= 2\int_0^\infty n_e^2(r)dy$, where r is measured from the center of the spherical expansion and y is measured along the line of sight. For a line of sight that passes at a projected distance b from the central source, the emission measure is proportional to b^{-3}. An exact integration shows the emission measure at projected radial distance b through a spherical wind to be

$$\mathrm{EM} = 2C^2 \int_0^\infty \frac{dy}{b^2 + y^2} = \frac{\pi C^2}{2b^3}\,, \tag{3}$$

where $C = \dot{M}_E/(4\pi\mu m_{\rm H} c_{\rm II})$ and y is the distance along the line of sight measured from the point of closest approach between the line of sight and the source. (We use the subscript E to denote parameters pertaining to an externally illuminated YSO.) A constant expansion velocity r^{-2} density profile produces an r^{-3} emission measure and projected radial intensity profile, roughly consistent with the observed radial profiles shown in Figure 11.

If we ignore absorption by dust in the H II region, the IF is located at a distance from the center of the clump, r_I, given by

$$F = \frac{Q}{4\pi d^2} = \int_{r_I}^\infty n_e^2(r)\alpha_B\, dr\,,$$

which leads to

$$r_I = \left[\frac{\dot{M}}{\mu m_{\rm H} v(r)}\right]^{2/3}\left(\frac{\alpha_B}{4\pi Q}\right)d^{2/3}\,.$$

The surface brightness of the ionized gas is proportional to the emission measure, EW $= \int n_e^2(L)dL$, where L is the line-of-sight path length. The ratio of the peak emission measure of a proplyd divided by that of the H II region is given by

$$\mathrm{EW}_p/\mathrm{EW}_{\rm H\,II} = \tfrac{1}{3}(r_{\rm S}/d)^2\,,$$

where $r_{\rm S}$ is the Strömgren radius of the H II region. O'Dell (1998) shows that the Hα surface brightness of the proplyds is bounded by the inverse square of the projected distance from θ^1 Ori C, providing strong evidence that the proplyd emission is dominated by photoionization.

If the externally illuminated YSOs are assumed to have identical power-law radial density profiles, $n(r) = n_0\, r^{-\alpha} = n_0(r_0)r_0^{\alpha}\, r^{-\alpha}$, the radius of the IF is expected to scale as

$$r_I = \left[\frac{(1-2\alpha)Q}{4\pi\alpha_B\, n_0^2(r_0)r_0^{2\alpha}}\right]^{1/(1-2\alpha)} d^{-2/(1-2\alpha)}\,,$$

which for $\alpha = 2$ gives $r_I \propto d^{2/3}$. A scaling $r_I \propto d^{1/2}$ implies a radial power-law index $\alpha = 5/3$. If the ionized density distribution is an exponential with $n(r) = n_0\, e^{-r/r_0}$, the formal solution for the location of the IF is

$$r_I = r_0 \ln\left[(2\pi\alpha_B\, r_0/Q)^{1/2} n_0\, d\right]\,,$$

where r_0 is the exponential scale height and n_0 is the density at location $r = 0$ of the coordinate system in which the position of r_I is measured. For the parameters of the Orion Nebula and an exponential scale height of $r_0 = 7\times 10^{14}$ cm (O'Dell 1998), this reduces to $r_I = r_0 \ln(0.87 n_6\, d_{17})$, where n_6 is the density in units of 10^6 cm^{-3} and d_{17} is in units of 10^{17} cm.

For spherical clouds with sufficient density to trap an IF, if the electron density outside the IF decreases as r^{-2}, then the electron density at the IF is given by $n_e(I) = (3Q/4\pi\alpha_B)^{1/2} r_I^{-1/2}\, d^{-1}$, where r_I is the cloud IF radius and d is the true (not projected) distance from θ^1 Ori C. So long as a cloud has sufficient density to shield itself from Lyman continuum radiation, the electron density at the IF is only determined by the geometry once steady state conditions are achieved. Since $n_e(I) \propto r_I^{-1/2}\, d^{-1}$, the peak surface brightness of the IF, which is proportional to its emission measure ($n_e^2\, L$), scales as d^{-2}. This is roughly consistent with the results given in Table 4. In principle, with precision calibration, the Hα images can be used to deduce the ratio of projected to true distance from θ^1 Ori C. For any given object, this yields two possible locations in three dimensions with respect to the ionizing star. Careful inspection of the images may be used to determine whether the object is in front of θ^1 Ori C or is in the background. In foreground objects, the circumstellar disks should be seen in silhouette against the externally illuminated YSO's own IF, and we are probably looking at the side of the disk that is not directly illuminated by θ^1 Ori C. In this case the disk should show up as a pure silhouette, even in the [O I] and in the near-IR H_2 lines. On the other hand, for externally illuminated YSOs in the background, the circumstellar disk will be located behind the YSO IF and not seen in silhouette. In this case we are probably seeing the face of the disk that is illuminated by soft UV radiation from θ^1 Ori C, which should result in bright near-IR H_2 lines and possibly [O I] emission from the irradiated disk face. Thus, it may be possible to derive the distribution of externally illuminated YSOs near Trapezium in three dimensions.

4.3. [O III] + Hα *Arcs*

HST images in the [O III] and Hα filters show arcs of emission lying between θ^1 Ori C and many externally illuminated YSOs at about 5% to 30% of the YSO–θ^1 Ori C distance. We propose that the [O III] + Hα arcs trace the shock structure formed by the interaction of the photoablated material expanding from the YSO IF (the "IF wind") with the stellar wind from θ^1 Ori C.

To be visible against the bright background of the Orion Nebula, the [O III] + Hα arcs must have an emission measure comparable to that of the nebula, which in Hα has an $n_e^2\, L$ of about 10^5–10^6 cm^{-6} pc toward Trapezium. If we assume that the [O III] + Hα arcs are seen predominantly where our line of sight is tangent to a sheet of emission, the path length through the emission region, L, is likely to be at most of order of the projected length of the emission region, or about 0.002–0.01 pc (corresponding to a projected length of 1″–3″). To produce an observed surface brightness comparable to the nebula, the density in the emission region must be at least of order 10^4 cm^{-3}. The density of the θ^1 Ori C stellar wind declines with distance as $\dot{M}_w/4\pi\mu m_{\rm H} d^2 v_w \approx 0.5\dot{M}_{-7}\, d_{17}^{-2}\, v_3^{-1}$ cm^{-3}. Upon passing through an adiabatic shock, the density only increases by a factor of 4. Thus, the observed [O III] + Hα arcs cannot correspond to the stellar wind shock itself, since the emission measure from this region is too low by many orders of magnitude.

We propose that the [O III] + Hα arcs are produced in a dense layer where the IF wind is compressed by a mild reverse shock associated with the stationary bow shock structure formed where the IF wind reaches ram pressure balance with the θ^1 Ori C stellar wind. Two physical mecha-

nisms may contribute to the [O III] and Hα emission of this layer: photoexcitation and turbulent mixing of this layer with the hot, shock-heated stellar wind debris (Begelman & Fabian 1990; Slavin, Shull, & Begelman 1993).

A stationary shock structure is formed around each externally illuminated YSO where the ram pressure of the IF wind equals the ram pressure of the θ^1 Ori C stellar wind (see Fig. 10). As discussed above, the gas flowing away from the IF acts to first order as a spherically symmetric wind with

$$n_E = \frac{\dot{M}_E}{4\pi d_E^2 \mu m_{\rm H} v_E}, \quad (4)$$

where d_E is the distance from the low-mass YSO, $\dot{M}_E \sim 10^{-7}\ M_\odot\ {\rm yr}^{-1}$ as given by equation (3), and v_E is about 1–2 times the sound speed in ionized gas (10–20 km s^{-1}). (Again, we use the subscript E to denote parameters pertaining to an externally illuminated YSO.) A similar formula holds for the massive stellar wind from θ^1 Ori C with $\dot{M}_w \sim 4 \times 10^{-7}\ M_\odot\ {\rm yr}^{-1}$ and $v_w \sim 1 \times 10^3$ km s^{-1} (Howarth & Prinja 1989). On the axis connecting the massive star and the externally illuminated YSO, ram pressure balance is reached when

$$\frac{d_E}{d_w} = \frac{\dot{M}_E v_E}{\dot{M}_w v_w} \approx 0.1\ . \quad (5)$$

Cantó, Raga, & Wilkin (1996) present analytic formulae that describe the shape of a bow formed at a wind-wind collision interface. Their formulae can be used to show that for conditions appropriate to the collision between the externally illuminated YSO ionized photoablation flow and the θ^1 Ori C wind, the separation between the externally illuminated YSO and the stagnation point in the bow shock, d_E, is about 0.05–0.2 times the separation between this point and θ^1 Ori C.

In general, we view the externally illuminated YSO and its bow shock along lines of sight that are inclined with respect to the line connecting the externally illuminated YSO and θ^1 Ori C, and we see a bright arc in projection from a portion of the bow shock structure where our line of sight is nearly tangent to the shock structure. The observed projected separation between the externally illuminated YSO and the arc is always larger than the projected separation between the YSO and the apex of the bow (which lies on the line connecting the YSO with θ^1 Ori C). For the estimated parameters of the IF winds and θ^1 Ori C, the predicted location of the bow shock closely matches the observed location of the [O III] + Hα arcs with a projected $d/L \approx 0.2$.

While the shock into the θ^1 Ori C stellar wind is too tenuous to produce observable amounts of [O III] + Hα emission, the density behind the reverse shock propagating into the externally illuminated YSO photoablation flow may be high enough ($n \sim 10^3$–10^4 cm^{-3}) to provide the required emission measure. However, this shock is propagating at less than 30 km s^{-1}, the expansion velocity of the externally illuminated YSO wind far from the IF, and is too weak to directly excite either Hα or [O III] emission. The compressed postshock layer may produce [O III] and Hα by two mechanisms: photoionization by the UV radiation from θ^1 Ori C, and excitation in a turbulent mixing layer formed by the mixing of the dense and cold (10^4 K) gas with shocked and hot (10^6 K) stellar wind. The externally illuminated YSO wind shock is expected to be isothermal since it is a weak shock, and the temperature of the preshock and postshock layers will be determined by photoionization equilibrium. Thus, the compression ratio will be roughly given by the Mach number squared, or about 4–10. At a distance of 1″ to 2″ from an externally illuminated YSO (where most [O III] arcs are seen), the IF wind has a density of about 10^2–10^3 cm^{-3}, and the postshock density will range from 10^3 to about 10^4 cm^{-3}. When this layer is nearly tangent to our line of sight, enhanced Hα emission and, to some extent, [O II] and [O III] emission will be observable, since the emission measure will be comparable to that of the nebular background.

There are several predictions that follow from this interpretation of the [O III] arcs. First, the arcs should be stationary structures that show no proper motion. Second, these shocks represent standing surfaces through which gas flows. Therefore, the radial velocity of Hα or [O III] in the arcs, which traces the motion of individual atoms or ions, should show Doppler shifts that are characteristic of the externally illuminated YSO wind—about 20 to 30 km s^{-1}. The postshock stellar wind in the bow shock skirts will preserve a large fraction of the 10^3 km s^{-1} velocity of the massive stellar wind. The postshock IF wind may be in part entrained by this hot plasma. Such entrainment, and the turbulent mixing that should result, will increase both the line width and the Doppler shift of the mixed gas. In this case, the [O III] arcs are expected to have a low Doppler shift with respect to stationary photoionized gas in the Orion Nebula if turbulent mixing does not play an important role. If turbulent mixing does play an important role, then the [O III] arcs are expected to have a large (up to several hundred km s^{-1}) radial velocity and a large line width.

Henney et al. (1996) proposed that the ionizing radiation from θ^1 Ori C reaches the disk surface. The collision between the resulting disk wind and the stellar wind from θ^1 Ori C produces a standing shock where ram pressure balance is reached. Henney et al. identify the bright hemispherical edges with the reverse shock ("Mach disk") formed where the IF wind passes through a roughly stationary shock. This model appears to be incorrect for several reasons: The azimuthally averaged radial profiles of surface brightness are consistent with photoionization models (cf. Sutherland 1997) of these edges and *not* with shock models. Furthermore, the observations provide no evidence of photoionization of the disk surface or the region between the disk and the emission-line crescents. If the IFs are identified with the hemispherical arcs, then the implied pressure of this region is greater than the ram pressure of the stellar wind, and wind-wind interactions should be expected to occur at a considerably greater distance from the externally illuminated YSO.

4.4. *Role of Thermal Conduction*

O'Dell (1998) argues that an exponential radial intensity profile provides a slightly better fit to the Hα emission profiles of some proplyds than does a power law. However, the differences are subtle, and both types of profile imply steep density and pressure gradients that will drive mass flows from the proplyds unless there is an external force that keeps the fluid in place. Three distinct physical effects can produce deviations from an r^{-3} intensity profile expected in a spherically expanding envelope: (1) Close to the IF, the

ionized fraction declines because of the decreasing flux of Lyman continuum photons. (2) Isothermal flows accelerate logarithmically, producing density profiles steeper than r^{-2} and intensity profiles steeper than r^{-3}. (3) Thermal conduction from the hot stellar wind bubble that may surround some proplyds will tend to accelerate the outer parts of the diverging photoablation flows. The first effect tends to lower the observed surface brightness just outside the IF. Both the second effect and the third effect lower the surface brightness at large radii when compared with an isothermal, fully ionized, and constant-velocity flow. These three effects produce radial intensity profiles that deviate below the r^{-3} radial dependence both near the IF and at large radii. Such profiles can approach an exponential form.

Externally illuminated YSOs located beyond the reverse shock of the θ^1 Ori C stellar wind will be embedded in the hot, postshock stellar wind bubble. The photoevaporating YSO environment is very similar to the spherical cloud considered by Cowie & McKee (1977) and McKee & Cowie (1977) in their treatment of thermal evaporation of clouds embedded inside 10^6–10^8 K bubbles produced by supernovae and stellar winds. Thermal conduction will, to first order, result in strong deviations from the isothermal expansion of the photoionized material that flows through the externally illuminated YSO IF. As shown by McKee & Cowie (1977) and Balbus & McKee (1982), the temperature of the photoionized plasma rises from its initial value of 10^4 K at some inner boundary to the temperature of the wind bubble as $r^{2/5}$ in the limit that the flow remains subsonic relative to the local sound speed. The thermal conduction–powered mass-loss rate is independent of the density of the wind bubble, but it does depend on its temperature and on the radius of the cloud according to $\dot{M} \approx 1.3 \times 10^{-7} T_7^{5/2} r_{-3} (30/\ln\Lambda)\ M_\odot\ \mathrm{yr}^{-1}$, where Λ is the Coulomb logarithm, T_7 is the bubble temperature in units of 10^7 K, and r_{-3} is the radius of the evaporating cloud in units of 10^{-3} pc (McKee & Cowie 1977).

Thermal evaporation becomes significant when the conduction-induced mass-loss rate at a cloud radius r_p becomes comparable to the radiation-induced mass-loss rate of the externally illuminated YSO. Conduction-induced mass loss becomes comparable to the estimated photoablation rate at a cloud radius of about 200 AU, comparable to the radii of the IFs at large distances from θ^1 Ori C. Thus, at a distance of more than about 200 AU, thermal conduction may dominate the flow characteristics.

Thermal conduction results in a radial temperature gradient, which leads to a more rapidly declining radial density profile than is characteristic of an isothermal flow. As shown by McKee & Cowie (1977), an exponential density profile is expected, and this will result in an exponential radial intensity profile. Therefore, large externally illuminated YSOs embedded in the hot stellar wind bubble are expected to have exponential radial intensity profiles. As discussed by O'Dell (1998), some externally illuminated YSOs exhibit significant deviations from the r^{-3} intensity profiles expected for an isothermal flow, and some objects can be fitted reasonably well with exponential radial intensity profiles. Future studies of the radial intensity gradients of embedded condensations might be used to map the extent of the thermal wind bubble.

4.5. *FUV Radiation*

Soft UV radiation with wavelengths between 912 and $\sim$2000 Å penetrates into the neutral gas between the YSO and the IF, establishing a photon-dominated (or photodissociation) region (PDR; Tielens & Hollenbach 1985). The intensity of soft UV radiation in the core of the Orion Nebula is about $G_0 = 10^5$ in units of the mean energy density of soft UV radiation in the vicinity of the Sun (about 1.6×10^{-3} ergs cm^{-3}, also known as the Habing field). Soft UV is primarily attenuated by dust, which, between 1000 and 2000 Å, produces about 3 to 5 mag of extinction for every 1 mag of visual extinction (A_V). Thus, the soft-UV energy density drops to solar-vicinity values when A_V is 2–3 mag, which for a standard gas-to-dust ratio corresponds to a hydrogen column density of (2–3) $\times 10^{21}$ cm^{-3}. The soft UV radiation field heats the gas in the PDR to temperatures of order 10^2–10^3 K with corresponding sound speeds of 1–3 km s^{-1} (Hollenbach & Störzer 1998). For any configuration that is in approximate hydrostatic balance prior to irradiation, the soft-UV heating will drive an outward expansion of gas at approximately the local sound speed. This expansion is fueled by the reservoir of material in the YSO environment and can maintain a static (in the frame of the YSO) IF at r_I for as long as the reservoir can sustain the FUV-powered disk wind (Johnstone et al. 1998).

Johnstone et al. (1998) present a model for externally illuminated YSOs in which the FUV radiation powers a wind expanding from the disk surface. The resulting disk mass-loss rate is of order $\dot{M}_E = 1.3 \times 10^{-7} \epsilon r_{d,15}\ M_\odot\ \mathrm{yr}^{-1}$ at a velocity $v_E \approx 3$ km s^{-1} (the expected sound speed in the PDR), where ϵ is a parameter of order unity and $r_{d,15}$ is the outer radius of the disk in units of 10^{15} cm. By the time this flow reaches several disk radii, it is approximately spherical. The column density between the disk outer radius r_d and the IF at r_I is given by

$$\mathrm{N(H)} \approx \frac{\dot{M}_E}{4\pi\mu m_{\mathrm{H}} v_E r_E} \approx (1\text{–}3) \times 10^{21} v_3^{-1} r_{10}^{-1}\ \mathrm{cm}^{-2}\,, \quad (6)$$

where v_3 is the flow velocity in units of 3 km s^{-1} and r_{10} is the point to which the column density is being estimated in units of 10 AU as measured from the central star.

The disk wind is self-regulating. If the column density between the disk and the IF is decreased, the flux of soft UV radiation incident on the disk will increase and result in a higher mass-loss rate. This pushes the IF outward until N(H) settles down at a value close to that given above. If this column density is much larger (as must be the case when the YSO is first exposed to UV radiation), too little soft UV radiation reaches the disk and the mass-loss rate is low. The D-type IF advances into the externally illuminated YSO envelope until a sufficient flux of soft UV radiation is available at the disk surface to stall the IF in the frame of the externally illuminated YSO. In steady state, the propagation velocity of the IF into the neutral photoablation flow exactly equals the outward velocity of the photoablated disk wind.

4.6. *Implications of* O I *Emission*

Our WFPC2 images of the Orion Nebula externally illuminated YSOs show that many contain disklike features that appear as dark silhouettes in [O III], [S II], [N II], Hα, and the continuum but are bright in [O I]. The best examples are HST 10 and 17, shown in Figure 5, which have an [O I] surface brightness of about 8×10^{-14} ergs s^{-1} cm^{-2} arcsec^{-2} (cf. Tables 3 and 4).

In principle, it is possible for the 6300 Å [O I] line to

resonantly scatter incident radiation. The maximum surface brightness caused by scattering is roughly $S = 1.8 \times 10^{-14} \eta_s d_{17}^{-2} (\Delta\lambda/\lambda) L_5$ ergs s^{-1} cm^{-2} arcsec^{-2} for a line width of 1 km s^{-1}, where we have assumed that the 6300 Å flux emitted by the Trapezium stars is approximately given by $(\Delta\lambda/\lambda)L_5$, where $L_5 = 10^5\ L_\odot$ is the Trapezium luminosity and η_s is the scattering efficiency. For [O I] line widths of order 4–5 km s^{-1}, the observed peak surface brightness of the [O I] emission from the silhouettes lies close to this value, so if it is produced by scattering, the scattering optical depth must be about unity. However, the scattering cross section for this forbidden transition is extremely low, requiring an O I column density of order $N(\text{O I}) \approx 2 \times 10^{21} b_{\text{kms}}$ cm^{-2} for an optical depth $\tau \approx 1$. Here b_{kms} is the line-broadening parameter in units of km s^{-1}. For normal metallicity this requires $N(\text{H}) \approx 10^{24}$ cm^{-2}. Unless the dust is depleted by a factor of order 10^3, the observed [O I] emission cannot be produced by scattering.

We now consider the excitation of [O I] by thermal collisions. Collisions with a kinetic energy of 1.97 eV are required to pump the 6300 Å [O I] transition. For a Maxwellian distribution, this requires that the mean kinetic energy of the collision partners be at least 0.5 eV, corresponding to a temperature of about 3800 K. In the midplane of the disk, the temperature is likely to be nearly in thermodynamic equilibrium with the incident radiation field. If the YSO embedded in the disk has luminosity L_{YSO}, the disk temperature is dominated by the central star for disk radii smaller than $r_d = d(L_{\text{YSO}}/L_5)^{1/2} \approx 1.3 \times 10^{15} [L_5/(1\ L_\odot)]^{-1/2}$ cm, beyond which the minimum disk temperature is set by the luminosity of Trapezium at about $T_d = 87 L_5^{1/4} d_{17}^{-1/2}$ K, where L_5 is the luminosity of the illuminating source in units of $10^5\ L_\odot$ and d_{17} is the distance from this source in units of 10^{17} cm. The disk midplane temperature at the radius where the escape speed is equal to the sound speed in ionized gas is about $T(r_G) \approx$ 100 K for a Sun-like star. However, FUV photons with energies in the range 6–13.6 eV can penetrate and heat regions where the column density is less than about $N(\text{H}) \approx 3 \times 10^{21}$ cm^{-2}. Models of photon-dominated regions predict temperatures of about 1000 K for FUV radiation fields in the range $10^4 < G_0 < 10^6$ (Tielens & Hollenbach 1995; Johnstone et al. 1998; Hollenbach & Störzer 1998). Burton, Hollenbach, & Tielens (1990) show that in very dense PDRs, a thin surface layer immediately adjacent to the IF with $N(\text{H}) < 10^{20}$ cm^{-3} can be heated to about 3000 K primarily by H_2 vibrational heating, in which photoexcited states of H_2 are collisionally de-excited and heat the medium.

HST 10 lies at a projected distance of 57″ (4×10^{17} cm) from θ^1 Ori C. The FUV flux from θ^1 Ori C at this distance is calculated to be $G_0 = 5 \times 10^4$. The Burton et al. (1990) model for $G_0 = 10^5$ and $n = 10^7$ cm^{-3} predicts a total 6300 Å [O I] flux of 3×10^{-16} ergs s^{-1} cm^{-2} in a PC pixel, about twice the peak surface brightness near the substellar point on the IF of HST 10. Thus, the [O I] emission located near the IF probably traces the component of very hot gas mentioned above. Our observations also show a second component of [O I] emission associated with the silhouette in HST 10, which presumably lies at the *base* of the PDR. The electron density at the HST 10 IF is estimated to be about 8×10^4 cm^{-3}. Assuming that the neutral hydrogen density inside the IF remains at least this high, the column density of H between the IF and the silhouette surface is at least about $nL = 4 \times 10^{20}$ cm^{-2}, where L is the separation between the silhouette's surface and the IF (about 5×10^{15} cm, corresponding to 0.″7.)

We propose that the [O I] emission is excited by 2 eV collisions with nonthermal particles that are not in thermodynamic equilibrium at the PDR temperature. There are two physical mechanisms in a PDR that may produce such a non-Gaussian high-energy tail on the Boltzmann distribution: the ejection of electrons from grains by the photoelectric effect and the dissociation and reformation of H_2 on grain surfaces. The photoelectric effect of FUV radiation produces electrons with energies ranging from 0 to about 6 eV that can suffer many elastic collisions with neutrals in the weakly ionized PDR prior to reaching an equilibrium distribution. Photoelectrons have sufficient kinetic energy to excite the [O I] line. The formation of H_2 on grain surfaces releases the 4.8 eV binding energy of molecular hydrogen. About half of the time, a recently formed H_2 molecule is ejected from the grain surface with an energy greater than 2 eV, also sufficient to excite [O I]. Thus, in the H_2–H I transition zone, where the destruction of H_2 is in approximate equilibrium with reformation, the total reformation rate will be comparable to the flux of photons absorbed in the Lyman and Werner bands of H_2. These two processes might produce a sufficient population of suprathermal particles to excite the observed [O I] emission. A detailed analysis of these processes will be presented elsewhere. A consequence of this model is that any abundant neutral species that has a transition to the ground state in the optical portion of the spectrum should produce detectable emission from the surface of the silhouettes embedded in the bright externally illuminated YSOs.

If the illuminating flux is about $G_0 = 10^4$, the observed surface brightness of the [O I] emission implies that the efficiency of conversion of incident FUV flux in the 6–13.6 eV range into [O I] line emission is about $[\epsilon(\text{[O I]}) \sin i]/G_{\text{FUV}} \leq 10^{-4}$, where $\epsilon(\text{[O I]})$ is the [O I] emission from the disk surface in ergs s^{-1} cm^{-2}, sin i is a correction for foreshortening, and G_{FUV} is the incident FUV radiation field. Assuming that the FUV radiation responsible for generating the [O I] emission is absorbed in a column density of hydrogen of order $N(\text{H}) \approx 10^{21}$ cm^{-2} and that the layer is no thicker than a PC resolution element (0.″05), the density in this layer is at least $n(\text{H}) \geq 3 \times 10^6$ cm^{-3}, or about 1 order of magnitude greater than the density at the IF.

The absence of forbidden line emission from other species in the [O I] emission zone associated with the silhouettes places another constraint on the physical characteristics of this region. The [O III], [N II], and [S II] lines originate in states that lie about 2 eV above the ground state and therefore have similar excitation requirements as [O I]. Since sulphur has an ionization potential of about 10.3 eV, the FUV photons will photoionize this species, and S II should be present in the PDR. Since the red [S II] lines require collisions of about 1.8 eV to excite, collisions that excite [O I] will also excite [S II]. The absence of red [S II] emission implies that sulphur is mostly in its neutral state, despite the presence of an intense FUV radiation field. This, in turn, implies that the recombination rate exceeds the photoionization rate. Using the recombination rate coefficients of Shull & Van Steenberg (1982), which give $\alpha_{\text{S II}} = 1.75 \times 10^{-12}\ T_3^{-0.63}$ cm^3 s^{-1}, where T_3 is the temperature

in units of 10^3 K, and the photoionization cross section of Verner & Yakovlev (1994) which gives $\sigma_{S\,I} = 1.63 \times 10^{-16}$ cm^2, and assuming a fractional electron abundance, $x_e = 10^{-4}$, this leads to

$$\frac{n_{S\,II}}{n_{S\,I}} = \frac{F_{FUV}\,\sigma_{S\,I}}{n_e\,\alpha_{S\,II}\,h\nu} = \frac{9 \times 10^{11}}{n_H}\,F_{12}\ \mathrm{cm}^{-3}\ ,$$

where F_{12} is the UV photon flux in units of 10^{12} photons s^{-1} cm^{-2}. At the high-density base of the PDR, the Lyman and Werner bands of H_2 block about half of the incident photons above the ionization threshold for S I and dust attenuates the radiation field by about a factor of 10–100. If recombinations deplete the S II, then the density in the [O I] emission zone must be around $n_H = 10^{10}$ cm^{-3} or higher. In the high-density and heated environment of the disk surface, it is possible that chemical reactions, such as those that lead to the formation of SO, also contribute to the depletion of S II, or may produce O I in the metastable state.

4.7. *Tails*

Observations of the 150 objects embedded within the Orion Nebula show that most externally illuminated YSOs have tails with lengths ranging from 0.″1 to about 4″, with a median length of about 0.″8. *There is no systematic dependence of tail length on projected separation from the primary illuminator.* The tails connect smoothly to the IFs that face the primary source of radiation and, in most objects, point directly away from the primary illuminator. The tails associated with sources lying within a projected distance less than 1′ of θ^1 Ori C point to this star to better than a few degrees. However, there are several sources between θ^1 Ori C and θ^2 Ori A that have very stubby tails with an axis of symmetry that tends to bisect the lines pointing to these sources. In these objects, the tail orientations may reflect the influence of irradiation by both stars. Most tails have sharp tips at the substellar point (the end of the tail most distant from the illuminator). The tail shapes are well represented by a conical shape linking the tips with the forward-oriented IFs. In the well-resolved tails, the IFs appear limb-brightened with some evidence for excess obscuration just inside the IF in the [N II] and [O III] images. The tails lying close to θ^1 Ori C tend to be long and skinny since the projected radius of the forward-facing IF decreases with decreasing projected distance from the illuminating source.

We have considered a variety of mechanisms for tail production; however, we do not have a satisfactory explanation for their existence at this time. We list some possible models and mechanisms for tail production and briefly discuss their problems.

Radiation pressure.—The Trapezium cluster has a total luminosity of about $10^5\ L_\odot$, and θ^1 Ori C has a Lyman continuum luminosity of about $Q = 1.5 \times 10^{49}$ photons s^{-1}. Soft UV and longer wavelength radiation couples strongly to dust, which exerts radiation pressure on the medium. This coupling is complex because of the role that grain charging plays in coupling the gas to the grains. The radiation pressure is given by $P_{rad} = L_*/4\pi c d^2 \approx 10^9 d_{17}^{-2}\ L_{*,5}$ cm^{-3} K, where L_* is the illuminator luminosity and $L_{*,5}$ is this luminosity in units of $10^5\ L_\odot$, and d_{17} is this distance in units of 10^{17} cm. The drift velocity of maximally charged grains through the gas is estimated to be of order 0.1 km s^{-1} for the typical conditions in externally illuminated YSOs in the Orion Nebula (Spitzer 1978). Radiation pressure effects are likely to be important only in regions where the effect of other forces produces velocities less than this drift velocity. Since the FUV radiation heats gas to about 10^3 K, where the sound speed is around 3 km s^{-1}, radiation pressure is expected to play only a minor role in tail formation.

Impact of stellar winds.—The cometary shapes of the tails suggest that they may be formed by wind-wind interactions (Dyson 1968, 1973). However, the IF wind discussed previously will shield the IF from direct impact by the stellar wind. Within 30″ of θ^1 Ori C, the Hα + [O III] arcs provide evidence that the IF outflow interacts with the θ^1 Ori C wind in a zone well separated from the IF. Though the postshock gas produced by these bow shocks may flow past the tails at subsonic velocities, the stellar winds are not likely to directly impact the tail region.

Radiative "breaking" of disks.—F. Bertoldi (1997, private communication) has suggested that when the pressure of the IF ($>10^9$ cm^{-3} K) exceeds the midplane pressure in the circumstellar disk, the disk material will be accelerated by the rocket effect. This material will be pushed into the region of the tail. Since the disk has angular momentum about its central star, it is hard to see how the observed pointed tails can be produced by this mechanism alone.

IF shadow.—Assume that the YSO is only surrounded by a circumstellar disk during initial ionization. Once steady state ionization is maintained, most of the photoablation occurs in the forward direction, the direction from which the bulk of the UV radiation is arriving. Gas that is shadowed from direct illumination can remain neutral. However, the diffuse radiation field will ionize this region quickly in the absence of rapid mass motions that can replenish the neutral medium.

PDR powered by the diffuse Lyman continuum.—Recombinations within an H II region effectively scatter Lyman continuum photons. For case B recombination, the diffuse radiation field has a total Lyman continuum luminosity about one-third that of the ionizing star. On average, the diffuse field is constant within the Strömgren sphere since most of it is formed by recombinations near the IF. Thus, on average the back side of a disk is exposed to a roughly constant flux $F_{diff} \approx \frac{1}{6}Q/4\pi r_S^2$, where r_S is the Strömgren radius of the H II region. This will heat the disk's back side to about 10^3 K, powering a PDR outflow at about 3 km s^{-1} from the portion of the disk where $r_d > r_G$, the radius at which the sound speed exceeds the local escape speed. Since the backflow is in the shadow of the disk and the forward-facing IF, it is ionized only by the diffuse radiation field at a rate that is roughly independent of location within the nebula. Thus, the tail may be a result of a PDR-induced flow from the shadowed back side of the disk. As the diffuse radiation field eats into the tail downstream from the disk, it becomes narrower, resulting in a conical shape and a sharp tip. The forward-facing IF radius decreases with decreasing distance from the illuminator. Thus, this model predicts that tails closer to the illuminator are shorter because of the smaller radius of the shadow zone, contrary to observation (Johnstone et al. 1998).

Leftover wind wakes.—It is possible that the tails are not formed by the present-day steady state processes, but rather by processes that operated prior to ionization, or by transient processes operating during initial ionization. High-mass stars produce powerful winds prior to photoionizing their environments. For example, the high-luminosity sources embedded in the BN/KL core behind the Orion Nebula produce one of the most spectacular protostellar outflows known. Dozens to hundreds of individual

"fingers" of shock-excited near-IR H_2 and [Fe II] emission indicate a poorly collimated flow at several hundred km s^{-1} from the high-luminosity region (Allen & Burton 1993; McCaughrean & Mac Low 1997). The Near Infrared Camera and Multiobject Spectrometer (NICMOS) Early Release Observations of the BN region reveal several hemispherical fronts close to BN that might be recent examples of fossil cloud cores surrounding embedded YSOs (Stolovy et al. 1998). When θ^1 Ori C was born, YSOs in its vicinity were likely surrounded by similar envelopes. Tails could have been forged from these envelopes by powerful outflows emerging from the young θ^1 Ori C, resulting in a dense wake downwind from θ^1 Ori C. Subsequent ionization of such a wake could produce the observed tails. The mass in the wake would be dependent on the formation history of the low-mass YSO, and probably independent of the projected distance from the high-mass star, readily explaining the observed independence of tail length on projected distance from the illuminator.

Initial ionization instability of a spherical envelope.—For circumstellar envelopes that have not been sculpted by a protostellar wind from a high-mass star, the transient stage of initial ionization may also produce a dense tail that may survive subsequent photoionization for a long time. Initial ionization of spherical clouds leads to cometary shapes since the downstream portion of the cloud is shielded by the upstream part of the cloud (Bertoldi 1989; Bertoldi & McKee 1990). For clouds with a power-law radial density profile with a negative index, the IF will decelerate and wrap around a condensation, eventually forming an isolated "teardrop" of neutral gas. To first order, the pressure gradient is always orthogonal to the IF. Therefore, the density contrast between a cloud and its surroundings is enhanced. The IF compresses gas downstream of the initial cloud centroid. Furthermore, the dense D-type IF is subject to a Vishniac type of instability (García-Segura & Franco 1996). IFs that wrap around an isolated dense clump will develop a tail whose density will be greatly enhanced by the compression of the IF and the rocket effect. Such tails may resist photoionization for a time comparable to that of the ages of the externally illuminated YSOs.

If the final two scenarios are correct, they provide evidence that most of the sources now having tails were surrounded by massive protostellar envelopes at the time of initial photoionization by θ^1C Ori. If so, tails provide evidence for the extreme youth of the Trapezium members that are now observed to be externally illuminated YSOs.

4.8. *Interpretation of the FOS UV Results*

The FOS spectra show a Lyα spike in the middle of a broad Lyα absorption feature at most observed positions. There is a layer of neutral H I in front of the Orion Nebula with a column density of about $N(\mathrm{H}) = 10^{20}$–10^{21} cm^{-2} that can be seen as an absorption feature against the nebular continuum in the 21 cm line and in a variety of optical absorption lines, such as sodium and magnesium (cf. O'Dell, Wen, & Hu 1993). The foreground H I is expected to produce a broad damped Lyα feature in the UV. The narrow Lyα emission spike superposed on this feature may be heliospheric emission that is backscattered by interstellar gas in the solar vicinity or geocoronal Lyα emission. However, it is also possible that a small fraction of the intrinsically very strong Lyα emission produced by the Orion Nebula leaks through the damped wings of the foreground H I layer. The visibility of nebular Lyα would be an indication that the foreground absorption component has a significantly different velocity than the emission produced by the Orion Nebula, consistent with determinations of the relative velocities of the nebular emission and foreground components observed at other wavelengths. The absence of the Lyα dip in the spectra pointed toward the externally illuminated YSOs implies that the background Lyα emission observed toward the SKY positions is absorbed by the externally illuminated YSO envelope. This may be evidence that, despite failure to attain perfect tracking with *HST*, our observations were pointed toward the neutral envelope of the externally illuminated YSOs.

The C IV feature observed in the FOS spectra is probably produced by scattering of the spectrum of θ^1 Ori C by dust along the line of sight. The observed full width of this feature, 18 Å, implies a stellar wind velocity of about 1600 km s^{-1} when the finite resolution of FOS is taken into account. This agrees well with previous determinations of the θ^1 Ori C stellar wind terminal velocity (1650 km s^{-1}; Franco & Savage 1982).

The FOC images demonstrate that in the UV silhouettes can be imaged with higher resolution and with lower contamination from the stellar continuum of the central stars than in the optical. The background continuum emission from the nebula is significantly stronger than at the longer wavelengths. The UV images show circumstellar silhouettes in several objects near θ^1 Ori C (Fig. 8). Their symmetric and elliptical appearance in the images provides evidence that these structures are circumstellar disks. The outer radii of these disks are typically several times smaller than the radii of the emission-line crescents that below are interpreted to be IFs.

5. DISCUSSION

5.1. *Evolutionary State and Mass of the YSO Environment*

Star formation in an interstellar gas cloud is not coeval. The duration of the star formation epoch can range from 10^5 to 10^6 yr in a given cloud core, to over 10^7 yr for an entire giant molecular cloud spawning an OB association. Herbig & Terndrup (1986), Jones & Walker (1988), and Hillenbrand (1997) have studied the age spread in the Trapezium cluster, finding few stars with evolutionary ages over 10^6 yr, a median stellar age of 3×10^5 yr, and some stars with ages as short as 10^5 yr. Thus, low-mass (0.1–3 $M_\odot$) star formation has been proceeding for about 10^6 yr in the OMC-1 cloud core. We therefore expect an age spread for the YSOs embedded in M42. The evolution of more massive stars proceeds faster than that of the lower mass members of the same cluster.

We estimate the minimum gas density required to form the stars present in the Trapezium cluster. If the 700 YSOs found within a radius of 1 pc of Trapezium have a mean mass of 0.8 $M_\odot$, the cluster has locked up about 560 $M_\odot$ in stars. This corresponds to an average minimum density needed to form these stars of $\langle n(\mathrm{H}_2)\rangle \approx 2 \times 10^3$ cm^{-3} in a radius of 1 pc. In the cluster core, the minimum gas density required would be about $\langle n(\mathrm{H}_2)\rangle_{\mathrm{core}} \approx 6 \times 10^5$ cm^{-3} based on the estimated density of 50,000 stars per cubic parsec (McCaughrean & Stauffer 1994) in the inner 0.1 pc cluster core. Recently Henney & Arthur (1998) reanalysed the Trapezium cluster core density, finding a value of 5×10^6 stars per cubic parsec. This average minimum density is a little below the current mean density of the ionized core of the Orion Nebula. However, the core average minimum density is comparable to the mean density of OMC-1, located

behind the nebula, and to the density of cores believed to be in the early phases of gravitational collapse in other regions of star formation. It is likely that the actual mean density of the core that formed the Trapezium cluster was more than 1 order of magnitude greater (2×10^4 to 10^7 cm^{-3}). The mean separation of stars in the core of the Trapezium cluster (roughly 0.02 pc, or 5000 AU) is smaller than the typical radius of star-forming cores in more isolated star-forming regions. These numbers imply that mutual interactions between YSOs and the cores from which they formed had a profound effect on their properties.

The cluster crossing time (nearly the same as the free-fall collapse time) is $\tau_c \approx (G\langle\rho\rangle)^{-1/2}$. If we use only the mass present in stars, τ_c is about 1.3 Myr for the entire cluster, but under 10^5 yr for the 0.1 pc cluster core. The cluster velocity dispersion, $\sigma_c \approx D_c(G\langle\rho\rangle)^{1/2}$, is expected to be about 1.5 km s^{-1} for the entire Trapezium cluster and 2.6 km s^{-1} for the core. If we assume that the initial gas density was 10 times greater, so that the star formation efficiency was only 10%, then $\tau_c \approx 0.4$ Myr for the entire cluster and less than 30,000 yr for the core. This results in a velocity dispersion of 5 km s^{-1} for the entire cluster and about 8 km s^{-1} for the core.

The median age of the Trapezium cluster (estimated to be 0.3–1.0 Myr) requires that it formed on a timescale comparable to or less than 1 free-fall time of the collapsing core. Stars now at the periphery have at most crossed the cluster a few times, but those within 0.1 pc of the core may have crossed several times. Thus, the scenario for star formation in this region is that a massive (a few times 10^3 $M_\odot$) core underwent supercritical collapse and fragmented within a free-fall time into about 700 stellar-mass subcores, which proceeded to form stars. Since the mean stellar separation in the Trapezium cluster is so small, it is likely that any residual cloud core material not rapidly accreted onto a protostar or its accretion disk was tidally or collisionally stripped in a crossing time and became part of lower density gas that was then dispersed by ionizing radiation.

At the onset of nebular ionization (which presumably prevents further gravitational collapse and star formation from undifferentiated gas because of the sudden increase of temperature and pressure by more than a factor of 100), YSOs in a variety of evolutionary stages were exposed. The stages range from cloud cores on the verge of collapse (Class −II or Class −I in the Boss 1995 terminology), to accreting protostars (Class 0), to objects containing YSOs (Classes I, II, and III in the Adams, Lada, & Shu 1987 terminology). This sequence represents a progression of decreasing gas mass in the circumstellar environment. In the global collapse scenario outlined above, any precollapse cores that may have survived are likely to be torn apart or accreted onto protostars, and unless there are YSOs in the region that predate this collapse, there has probably not been enough time for any YSO to evolve beyond the Class III stage. The evolutionary state and the mass of the YSO determine the amount of gas that will be present in the YSO environment when it is exposed to UV radiation and, possibly, stellar winds. The earlier the evolutionary state and the higher the mass, the more gas likely to be present when the external UV source turns on.

5.2. *Comparison with Other Star-forming Regions*

Hester et al. (1996) present *HST* WFPC2 images of the elephant trunks that lie several arcminutes southeast of the core of M16. In their discussion of the structure of several candidate YSOs in the region, they argue that the YSOs embedded in the Orion Nebula are also elephant trunks that are seen face-on. Their detached appearance should be a consequence of our point of view: we see the elephant trunks perfectly end-on. However, since externally illuminated YSOs are seen throughout the Orion Nebula, this interpretation is completely unlikely.

Hester et al. (1996) claim to have identified hundreds of stars in the M16 elephant trunks. Though claimed to be YSOs, none have been shown to posses any of the signatures of youth, such as outflows, infrared excess emission, or other characteristics of stellar youth. However, their images provide evidence for a few proplyd-like objects in the immediate vicinity of the elephant trunks that may contain YSOs.

C. Stapelfeldt (1997, private communication) has used *HST* to search several nearby H II regions for proplyd-like objects. These results have mostly proved negative, though a few possible candidates have been found in S155. Caulet (1997) reported finding one proplyd-like object in the Lagoon Nebula (M8) on *HST* archival images. Bally, Yu, & Devine (1998b) have searched the young H II region S106 for proplyds with *HST*, finding none. The sum total of these observations points to the uniqueness of the large collection of externally illuminated YSOs embedded in the Orion Nebula.

A large fraction of the YSOs in the core of the Orion Nebula are surrounded by extended circumstellar material. Within 20″ of Trapezium, about 80% of stars have retained their circumstellar material and are "proplyds." Upper bounds on the masses of the circumstellar material surrounding some of these YSOs have been determined by means of millimeter-wavelength interferometry by Mundy, Looney, & Lada (1995). Lada et al. (1996) report the detection of 1.3 mm wavelength continuum emission from three out of 12 externally illuminated YSOs near Trapezium, with masses in the range 0.007–0.016 $M_\odot$. Searches for 230 GHz ^{13}CO and continuum emission toward the large silhouettes 182−413 (HST 10), 183−405 (HST 16), and 114−426 with the Owens Valley Radio Observatory interferometer have resulted in upper bounds less than about 0.01 $M_\odot$ toward these and several other objects in the field of view (Bally et al. 1998a). These bounds are consistent with the lower bounds estimated from extinction (McCaughrean & O'Dell 1996; Chen et al. 1998). From the collection of available data, it is possible to conclude that the maximum mass of dusty circumstellar matter surrounding these YSOs is about 10^{-2} $M_\odot$, and for a typical mass-loss rate of 10^{-7} $M_\odot$ yr^{-1} the maximum lifetime of externally illuminated YSOs against photoablation is about 10^5 yr.

Star formation in the Orion Nebula may be representative of the typical environment in which most stars are born. We have a fairly complete census of molecular clouds, star-forming regions, and young stars within 500 pc of the Sun. At least 90% of all stars younger than 10 or 20 million years were formed within the boundaries of four major OB associations: Scorpius-Centaurus, Perseus OB2, Orion OB1, and Lacerta OB1 associations (cf. Blaauw 1991). While typical OB associations such as Sco-Cen and Orion produce about $(1–3) \times 10^4$ stars each during a 5–15 Myr period of star formation, isolated dark clouds such as Taurus produce fewer than 10^3 stars in a comparable time

interval. Most star formation in the OB associations occurs in short-duration "microbursts" during which the gravitational collapse of 10^3–10^4 $M_\odot$ cloud cores produce clusters of 50–1000 stars in less than 1 million years in a region smaller than 1 pc (Lada 1992; Lada, Alves, & Lada 1996; Bally, Devine, & Reipurth 1996). The birth of one or more massive stars, which heats, dissociates, and ionizes the remaining gas, may terminate star formation in such a region. If the fraction of mass converted into stars (the star formation efficiency) is less than about 30% of the initial mass, the resulting cluster of stars will be gravitationally unbound. Low-mass stars formed in OB associations are likely to be exposed to the harsh UV radiation and, in some cases, the stellar winds produced by massive O and early B stars, for a time ranging from 0.1 to 10 million years.

The detection of a large number of YSOs surrounded by what appear to be circumstellar disks may provide some constraints on the formation frequency of planets. If the externally illuminated YSOs are shown to be losing mass at the rates estimated above, and if these disks contain less than 0.01 $M_\odot$ of material, then they may be destroyed before forming planets. Furthermore, if most stars form in environments similar to the Orion Nebula, then planet formation may be relatively rare. On the other hand, it is possible that most YSOs that are now externally illuminated are sufficiently old that their disks have condensed or coagulated a large fraction of their solid matter into centimeter- or meter-sized objects that can resist photoevaporation and which may be hard to detect with present methods. In this case, our disk mass estimates may be severe lower limits, and the formation of protoplanets may proceed in environments like the Orion Nebula. Are the Orion Nebula YSOs surrounded by protoplanetary disks that have, or soon will, form new planets? Or will photoablation destroy the disks before they have had a chance to form new planets? Future studies of YSOs in the Orion Nebula and in other star-forming regions will determine whether planet formation is very rapid or rare.

6. CONCLUSIONS

We have presented 9–23 AU resolution *HST* Faint Object Camera and Planetary Camera images of several dozen YSOs embedded within the Orion Nebula that are surrounded by externally illuminated circumstellar material. We have presented peak surface brightness measurements in five filters centered on the [O III], [O I], Hα, [N II], and [S II] emission lines. We also have presented the first UV spectra and images of several objects. We have reviewed the observed properties of the YSO environments and presented an interpretation of the observed source structures and morphologies in terms of a dynamical model of external radiation-induced mass loss. The main results of this study are as follows:

1. Most YSOs within a 1′ diameter region centered on the Trapezium cluster are surrounded by bright emission-line crescents facing the massive stars in the region. In most objects, the crescents are hemispherical. The peak surface brightness of the crescents declines rapidly with increasing projected distance from θ^1 Ori C. We interpret the crescents as quasi-static ionization fronts with peak electron densities just outside these fronts ranging from $n_e = 10^5$ to 10^6 cm^{-3}. The emission flux ratios of the observed lines are consistent with photoionization models. Assuming that the thermal pressure in the IFs dominates the dynamics, the freshly ionized plasma is likely to expand away from the dense neutral condensation at about the sound speed of the ionized gas as an isothermal IF wind. The resulting r^{-2} density profiles are expected to produce r^{-3} emission-line intensity profiles that are in good agreement with the azimuthally averaged and background-subtracted Hα emmision-line gradients observed toward most objects. Estimated mass-loss rates are around $\dot{M} = 10^{-7}\,M_\odot$ yr^{-1}.

2. The Orion Nebula contains several types of filamentary structures bright in [O III] and Hα. About 50% of the externally illuminated YSOs within a radius of about 30″ of θ^1 Ori C are surrounded by arcs of [O III] and Hα emission on the side facing θ^1 Ori C. These arcs have typical radii ranging from 1″ to about 5″. We argue that the arcs concentric with externally illuminated YSOs trace the shock structure formed by the interaction of the isothermal flow from the crescent-shaped IFs surrounding the externally illuminated YSOs with the fast stellar wind ejected by θ^1 Ori C. Neither the reverse shock propagating into the low-velocity photoablation flow nor the stationary bow shock through which the θ^1 Ori C stellar wind must pass in moving past the obstacle presented by the YSO can excite the observed emission. However, a dense layer forms between these two shocks, and gas in this region can be excited either by UV radiation or by turbulent mixing with the hot postshock stellar wind. The [O III] and Hα filaments that are not concentric with IF crescents tend to have random orientations and are located far from stellar objects. This second class of filaments are likely to trace HH flows, which are shocks powered by high-speed stellar outflows or jets.

3. Externally illuminated YSOs located at a projected distance of more than 30″ from Trapezium tend to be larger than YSOs located closer to θ^1 Ori C. They lack concentric [O III] and Hα emission-line arcs. In a few objects, the radial intensity profiles can be well fitted by an exponential function. We argue that these objects are embedded in the hot bubble formed by the θ^1 Ori C stellar wind after it passed through a strong reverse shock. Thermal conduction can alter the structure of the photoablation flow at distances larger than about 200 AU from an embedded YSO by heating the outer parts of the expanding ionized envelope. The radial temperature gradient is expected to accelerate the flow, producing a steeper than r^{-2} density profile that may result in large deviations from r^{-3} intensity profiles.

4. Most externally illuminated YSOs have tails ranging in length from 0.″3 to over 4″ that point radially away from the source of illumination. There is no systematic dependence of tail length on projected distance from θ^1 Ori C. However, as the forward-facing IFs increase in radius, the approximately constant tail lengths lead to progressively stubbier looking objects. Tails trailing behind YSOs near θ^1 Ori C are long and skinny, while those behind sources located at large projected distances are short and stubby. Many tails are dusty and opaque and seen in silhouette against the nebular emission. Tail formation is not understood.

5. Many externally illuminated YSOs contain dark regions at their centers seen in silhouette in [O III], [N II], [S II], Hα, and the continuum. These silhouetted regions are concentric and symmetric about the central stars when the latter are visible in our images. The silhouetted regions may trace high-opacity circumstellar disks. The radius of the

silhouetted region is typically at least a factor of 2 smaller than the radius of the IF. In several of the larger objects, where the light of the central star does not interfere, the silhouetted regions are seen in *emission* in the [O I] line. This component of the [O I] emission is distinct from that arising from the IFs, whose intensities agree with the predictions of models of the photodissociation region. The absence of [S II] emission is used to derive a density of about 10^{10} cm^{-3} in the [O I] emission region at the disk surface. The excitation of the 6300 Å [O I] line requires 2 eV collisions, or temperatures of at least 4000 K. Soft UV radiation that can penetrate to the disk surface is not likely to be capable of producing temperatures sufficiently high to excite the [O I] emission. We argue that a nonthermal process, such as collisional excitation by a high-velocity tail of particles that are not in thermodynamic equilibrium, may be responsible for the [O I] excitation. Examples of possible excitation mechanisms include 2–6 eV electrons ejected from grains by the photoelectric effect, or suprathermal H_2 molecules ejected from grain surfaces where reformation has taken place.

In a companion paper (Johnstone et al. 1998) we show that photoheating of the embedded disk surface by the incident soft UV radiation field can drive a low-velocity and mostly neutral disk wind at a velocity of about 3 km s^{-1} with a mass-loss rate that is approximately independent of the distance from θ^1 Ori C. This wind is expected to drive the IF to several disk radii and has a mass-loss rate that closely matches that needed to explain the properties of the photoionized portion of the externally illuminated YSO environment.

We thank the staff at STScI for their excellent support. We thank C. Robert O'Dell for many thought-provoking discussions and the use of his ERO data. We also thank Hans Zinnecker, Dave Hollenbach, Mark McCaughrean, and John Dyson for useful discussions. We thank David Theil for extensive help with data reduction, figure production, and many interesting discussions. This work was conceived over a decade ago at a Santa Cruz star formation workshop during a lunchtime conversation between Hans Zinnecker and J. B. This work was partially supported by NASA grant GO-5469 from the Space Telescope Science Institute, which is operated by the Association of Universities for Research in Astronomy, Inc. under NASA contract NAS5-26555. J. B. was also partially supported by NASA grant NAGW-3192. R. S. S. would like to acknowledge the support of the NASA Astrophysical Theory Program at the University of Colorado (grants NAGW-766 and NAGW-1479).

REFERENCES

Adams, F. C., Lada, C. J., & Shu, F. H. 1987, ApJ, 312, 788
Allen, D. A., & Burton, M. G. 1993, Nature, 363, 54
Axon, D. J., & Taylor, K. 1984, MNRAS, 207, 241
Balbus, S. A., & McKee, C. F. 1982, ApJ, 252, 529
Bally, J., Devine, D., & Reipurth, B. 1996, ApJ, 473, L49
Bally, J., Devine, D., & Sutherland, R. A. 1995, in Circumstellar Disks, Outflows, and Star Formation, ed. S. Lizano & J. M. Torrelles (Rev. Mexicana Astron. Astrofis. Ser. Conf. 1) (México, D.F.: Inst. Astron., Univ. Nac. Autonoma México), 13
Bally, J., Testi, L., Sargent, A., & Carlstrom, J. 1998a, AJ, in press
Bally, J., Yu, K. C., & Devine, D. 1998b, in preparation
Begelman, M. C., & Fabian, A. C. 1990, MNRAS, 244, 26P
Bertoldi, F. 1989, ApJ, 346, 735
Bertoldi, F., & McKee, C. 1990, ApJ, 354, 529
Blaauw, A. 1991, in The Physics of Star Formation and Early Stellar Evolution ed. C. J. Lada & N. D. Kylafis (NATO ASI Ser. C, 342) (Dordrecht: Kluwer), 125
Boss, A. 1995, in Circumstellar Disks, Outflows, and Star Formation, ed. S. Lizano & J. M. Torrelles (Rev. Mexicana Astron. Astrofis. Ser. Conf. 1) (México, D.F.: Inst. Astron., Univ. Nac. Autonoma México), 165
Burton, M. G., Hollenbach, D. J., & Tielens, A. G. G. M. 1990, ApJ, 365, 620
Cantó, J., Raga, A. C., & Wilkin, F. P. 1996, ApJ, 469, 729
Castor, J., McCray, R., & Weaver, R. 1975, ApJ, 200, L107
Caulet, A. 1997, BAAS, 190, No. 41.14
Chen, H., Bally, J., O'Dell, C. R., Caughrean, M. J., Thompson, R. I., Rieke, M., Schneider, G., & Young, E. T. 1998, ApJ, 492, L173
Churchwell, E. B., Felli, M., Wood, D. O. S., & Massi, M. 1987, ApJ, 321, 516
Cowie, L. L., & McKee, C. F. 1977, ApJ, 211, 135
Dyson, J. E. 1968, Ap&SS, 1, 388
———. 1973, A&A, 27, 459
Felli, M., Churchwell, E. B., Wilson, T. L., & Taylor, G. B. 1993a, A&AS, 98, 137
Felli, M., Taylor, G. B., Catarzi, M., Churchwell, E. B., & Kurtz, S. 1993b, A&AS, 101, 127
Franco, J., & Savage, B. D. 1982, ApJ, 255, 541
Garay, G., Moran, J. M., & Reid, M. J. 1987, ApJ, 314, 535
García-Segura, G., & Franco, J. 1996, ApJ, 469, 171
Hayward, T. L., Houck, J. R., & Miles, J. W. 1994, ApJ, 433, 157
Hayward, T. L., & McCaughrean, M. J. 1997, AJ, 113, 346
Henney, W. J., & Arthur, S. J. 1998, AJ, in press
Henney, W. J., Raga, A., Lizano, S., & Curiel, S. 1996, ApJ, 465, 216
Herbig, G. H. 1974, PASP, 86, 604
Herbig, G. H., & Terndrup, D. M. 1986, ApJ, 307, 609
Hester, J. J., et al. 1996, AJ, 111, 2349
Hillenbrand, L. A. 1997, AJ, 113, 1733
Hollenbach, D., & Störzer, H. 1998, in preparation
Howarth, I. D., & Prinja, R. K. 1989, ApJS, 69, 527
Hu, X. 1996, Ph.D. thesis, Rice Univ.
Johnstone, D., Hollenbach, D., & Bally, J. 1998, ApJ, 499, 758
Jones, B. F., & Walker, M. F. 1988, AJ, 95, 1755
Lada, E. A. 1992, ApJ, 393, 25.
Lada, C. J., Alves, A., & Lada, E. A. 1996, AJ, 111, 1964
Lada, E. A., Dutrey, A., Guilloteau, S., & Mundy, L. 1996, BAAS, 189, No. 53.01
Laques, P., & Vidal, J.-L. 1979, A&A, 73, 97
Massey, R. M., & Meaburn, J. 1993, MNRAS, 262, L48
———. 1995, MNRAS, 273, 615
McCaughrean, M. J. 1988, Ph.D. thesis, Univ. Edinburgh
McCaughrean, M. J., & Mac Low, M.-M. 1997, AJ, 113, 391
McCaughrean, M. J., & O'Dell, C. R. 1996, AJ, 111, 1977
McCaughrean, M. J., & Stauffer, J. R. 1994, AJ, 108, 1382
McCullough, P. R., Fugate, R. Q., Chritou, J. C., Ellerbroeck, B. L., Higgins, C. H., Spinhirne, J. M., Cleis, R. A., & Moroney, J. F. 1995, ApJ, 438, 394
McKee, C. F., & Cowie, L. L. 1977, ApJ, 215, 213
Meaburn, J. 1986, A&A, 164, 358
———. 1988, MNRAS, 233, 791
Meaburn, J., Massey, R. M., Raga, A. C., & Clayton, C. A. 1993, MNRAS, 260, 625
Mundy, L. G., Looney, L. W., & Lada, E. A. 1995, ApJ, 452, L137
O'Dell, C. R. 1998, AJ, 115, 263
O'Dell, C. R., Hartigan, P., Bally, J., & Morse, J. A. 1997, AJ, 114, 2016
———. 1997, AJ, submitted
O'Dell, C. R., & Wen, Z. 1994, ApJ, 436, 194
———. 1995, ApJ, 438, 784
O'Dell, C. R., Wen, Z., & Hu, X. 1993, ApJ, 410, 696
O'Dell, C. R., & Wong, S.-K. 1996, AJ, 111, 846
Pogge, R. W., Owen, J. M., & Atwood, B. 1992, ApJ, 399, 147
Prosser, C. F., Stauffer, J. R., Soderblom, L. H. D. R., Jones, B. F., Werner, M. W., & McCaughrean, M. J. 1994, ApJ, 421, 517
Shull, J. M., & Van Steenberg, M. 1982, ApJS, 48, 95
Slavin, J. D., & Shull, J. M., & Begelman, M. C. 1993, ApJ, 407, 83
Spitzer, L. 1978, Physical Processes in the Interstellar Medium (New York: Interscience)
Sutherland, R. S. 1997, in ASP Conf. Ser. 121, Accretion Phenomena and Related Outflows, ed. D. T. Wickramasinghe, G. V. Bicknell, & L. Ferrario (San Francisco: ASP), 566
Sutherland, R. S., Bicknell, G. V., & Dopita, M. A. 1993, ApJ, 414, 510
Stolovy, S. R., et al. 1998, ApJ, 492, L151
Taylor, K., & Münch, G. 1978, A&A, 70, 359
Tielens, A. G. G. M., & Hollenbach, D. 1985, ApJ, 291, 722
Verner, D. A., & Yakovlev, D. G. 1995, A&AS, 109, 125
Warren, W. H., & Hesser, J. E. 1977, ApJS, 34, 115
Weaver, R., McCray, R., Castor, J., Shapiro, P., & Moore, R. 1977, ApJ, 218, 377